

STATISTICAL PREDICTIONS OF THE ACCRETED STELLAR HALOS AROUND MILKY WAY-LIKE GALAXIES

J. SEBASTIAN MONZON[✉], FRANK C. VAN DEN BOSCH[✉], AND MARTIN P. REY[✉]

Department of Astronomy, Yale University, PO. Box 208101, New Haven, CT 06520-8101 and

Department of Physics, University of Bath, Claverton Down, Bath, BA2 7AY, UK

Version January 28, 2026

ABSTRACT

In the Λ CDM paradigm, stellar halos form through the accretion and disruption of satellite galaxies. We introduce new semi-analytic modeling within the SatGen framework to track the ex-situ stellar components of Milky Way-like galaxies across large ensembles of merger trees, enabling a statistical study of the stochastic nature of galaxy assembly. We find that accreted stellar halos are typically built by only a few progenitors and are highly sensitive to the fate of the most massive satellite, producing order-of-magnitude variations in accreted stellar halo mass even at fixed host halo mass. Different stellar components trace distinct phases of host halo growth: central and accreted stellar mass correlate most strongly with early assembly, while surviving satellites trace more recent accretion. Finally, using Random Forest Regression, we quantify how well observable galaxy properties can recover halo assembly histories, providing a framework for interpreting upcoming low-surface-brightness observations of stellar halos.

Keywords: methods: analytical — methods: statistical — galaxies: satellites — galaxies: stellar halos — cosmology: dark matter

1. INTRODUCTION

According to the standard Λ CDM cosmological paradigm, galaxies form hierarchically through the accretion of lower mass satellites. As these satellites infall, they are subjected to disruptive tidal forces that strip their mass and enrich galactic halos with stellar debris. The ages, star formation histories, and kinematic properties of accreted satellites and their tidal debris therefore provide valuable insight into the assembly histories of their parent galaxies. Particularly for Milky Way like galaxies, the accreted stellar halo (ASH) component is an invaluable laboratory for learning about the earliest generations of stellar populations (Helmi 2020) and investigating the low-mass end of the galaxy-halo connection (Bullock & Johnston 2005; Wechsler & Tinker 2018; Sales et al. 2022; Rey & Starkenburg 2022; Forourhar Moreno et al. 2025).

Due to the long dynamical timescales in the outskirts of stellar halos, merger events can be preserved in the kinematic properties and chemical signatures of accreted halo stars. Using precision astrometry from the *Gaia* mission (see Deason & Belokurov 2024; Bonaca & Price-Whelan 2025, for recent reviews) observers have leveraged this fact and extensively studied the stellar halo of the Milky Way (MW) (e.g., Deason et al. 2015; Naidu et al. 2021; Malhan et al. 2022; Sharpe et al. 2024). Detailed studies in this subfield of “galactic archaeology” have uncovered the MW’s most recent major-merger – the Gaia Sausage Enceladus (GSE) system which is inferred to have been accreted ~ 10 Gyr ago (Belokurov et al. 2018; Helmi et al. 2018; Koppelman et al. 2018). This is consistent with the general consensus (Bullock & Johnston 2005; Bell et al. 2008; Cooper et al. 2010; Deason et al. 2016; Fattahi et al. 2019; Cooper et al. 2025) that the MW’s stellar halo was built up relatively quickly via a handful of massive merger events at early times.

Extrapolations from local measurements ($d_{\text{helio}} \lesssim 5$ kpc) give *total* mass estimates of $\sim 10^9 M_{\odot}$ for the MW’s stellar

halo (Deason et al. 2016, 2019; Malhan et al. 2022). Exactly what fraction of the stellar halo comes from stars formed in the main progenitor (“in-situ”) vs. stars formed in systems that were then accreted onto the main progenitor (“ex-situ”) is still very uncertain (Rodriguez-Gomez et al. 2016; Sanderson et al. 2018; Font et al. 2020). This uncertainty arises primarily because the dynamical evolution of galaxies tends to mix the two populations. For example, satellites on low-inclination orbits can deposit some of their stars in the disc (Abadi et al. 2003) or the bulge (Zhu et al. 2022). Similarly, stars that were born in the disc can be perturbed onto more energetic halo orbits (Zolotov et al. 2009; Tissera et al. 2013; Cooper et al. 2015).

Recent advances in wide-field, deep-imaging programs have begun the challenging work of contextualizing the MW’s specific formation scenario by focusing on the ultra-low surface brightness outskirts of galaxies outside of the Local Group. Instruments such as the Dragonfly Telephoto Array (Abraham & van Dokkum 2014) have demonstrated the capability to detect diffuse structures at extremely low surface brightness for a handful of galaxies (Merritt et al. 2016; Gilhuly et al. 2022). Complementary surveys such as the CFHT Large Area U-band Deep Survey (CLAUDS; Sawicki et al. 2019) and the Hyper Suprime-Cam Subaru Strategic Program (HSC-SSP, Aihara & the HSC Collaboration 2018) provide the photometric depth to systematically study the morphology of galaxy outskirts across cosmic time (Williams et al. 2025). Looking ahead, the upcoming ARRAKIHS mission (Guzmán 2024) is designed to push these studies to even lower surface brightness levels across larger samples of galaxies, promising a significant expansion in our knowledge of MW-like galaxy assembly.

Cosmological hydrodynamical simulations like Illustris (Elias et al. 2018; Merritt et al. 2020), EAGLE (Davison et al. 2020; Proctor et al. 2024), FIRE (Sanderson et al. 2018) and FOGGIE (Wright et al. 2024) provide crucial insights by capturing the complex interplay between baryonic processes and hierarchical formation, while still resolving low-mass systems.

These studies show that disrupted remains of accreted satellites are ubiquitous in the stellar halos of MW-like galaxies. These accretion events can manifest themselves as metallicity/age gradients in the density profiles of the halo (Font et al. 2020), dynamically heated inner regions of the halo (Zhu et al. 2022), or as populations of stellar streams or shells (Riley et al. 2024; Shipp et al. 2024). However, because these analyses use a variety of subgrid prescriptions to model star formation and stellar evolution, there is no consensus on the predicted accreted stellar mass budget across simulation suites (Sales et al. 2022). Furthermore, although modern zoom-in simulations Monachesi et al. (2019); Orkney et al. (2022); Celiz et al. (2025) can reach mass resolutions of $\sim 10^4 - 10^5 M_{\odot}$, they come at great computational cost, making it challenging to build up a statistically significant sample of MW-like halos (e.g., Engler et al. 2021). Finally, these analyses also suffer from numerical artifacts such as artificial disruption (van den Bosch et al. 2018; van den Bosch & Ogiya 2018; Errani & Peñarrubia 2020) and uncertainties associated with subhalo finding algorithms (Diemer et al. 2024; Mansfield et al. 2024; Kong et al. 2025). Together, these issues limit the use of hydrodynamical simulations in isolating and studying the impact that different mass accretion histories have on present-day stellar halos. Complementary modeling approaches are therefore needed to efficiently explore large ensembles of MW-like systems without compromising control over the relevant physical parameters.

In this paper, we use the semi-analytic model `SatGen` to investigate the correlations between the mass accretion histories (MAH) of MW-like galaxies, the stellar mass of the ASH, and the surviving populations of satellite galaxies. Instead of modeling the orbits of star particles post accretion (Dropulic et al. 2025), we develop a computationally-inexpensive and flexible framework that outputs realistic galactic properties. We apply this framework to large samples of MW-like merger trees. Given the significant halo-to-halo variance inherent in surviving populations of satellite galaxies (Monzon et al. 2024), it should come as no surprise that accounting for variance in the *disrupted* populations of satellite galaxies is critical (Deason et al. 2016; Harmsen et al. 2017; Cooper et al. 2025). The main goal of this work is to understand what shapes the ASHs of MW-like galaxies without relying on galaxy–halo connection prescriptions that are specific to any single simulation suite, and to test the efficacy of inferring MAHs from observables.

This paper is organized as follows: Section 2 presents a detailed description of our semi-analytic framework and the assumptions that go into modeling the stellar halos. Section 3 presents our fiducial results and describes how different sources of stochasticity impact the populations of surviving and disrupted satellites. Section 4 investigates the correlation strengths between properties of the ASH, the surviving satellite population, and the MAH of their host halos. We finish with a discussion of our main results in Section 5 and a summary of our conclusions in Section 6. Throughout, we adopt a flat Λ CDM cosmology with a present-day matter density $\Omega_m = 0.3$, a baryon density $\Omega_b = 0.0465$, power spectrum normalization $\sigma_8 = 0.8$, spectral index $n_s = 1.0$, and a Hubble parameter $h = (H_0/100 \text{ km s}^{-1} \text{ Mpc}^{-1}) = 0.7$, roughly in agreement with the Planck18 constraints (Planck Collaboration et al. 2020).

2. METHODOLOGY

Our analysis employs the `SatGen` code (Jiang et al. 2021; Green et al. 2021), a state-of-the-art, semi-analytical model (SAM) devised to generate statistical samples of satellite galaxy populations. Briefly, `SatGen` constructs merger trees for host halos for a given cosmology using the extended Press-Schechter (EPS) method of Parkinson et al. (2008). These merger trees describe the complete MAHs of all progenitor halos that merge over time to produce a final host halo and are in excellent agreement, in a statistical sense, with merger trees extracted from N -body simulations (Jiang & van den Bosch 2014; van den Bosch et al. 2014). `SatGen` assigns stellar masses and sizes to progenitor halos at accretion and integrates their orbits accounting for dynamical friction and tidal stripping using semi-analytic prescriptions that are calibrated against a large suite of DMO high-resolution idealized simulations. Throughout the process, we keep track of how much stellar mass each satellite loses due to tides, which ultimately contributes to the final ASH of the host halo system.

2.1. Merger Trees

Throughout, we use three distinct samples of merger trees for MW-like halos taken from Monzon et al. (2024). These have present-day masses that are drawn from a log-normal distribution centered on $M_{\text{DM}} = 10^{12} M_{\odot}$ and with a scatter of σ_M dex. For the first sample, S_0 , we set $\sigma_M = 0$ so that all host halos have exactly the same halo mass of $10^{12} M_{\odot}$. The subsequent samples, S_{15} and S_{30} , were constructed with $\sigma_M = 0.15$ and 0.30 dex, respectively. Each merger tree sample is made up of 10,000 unique accretion histories, yielding a total of 30,000 galaxies and an excellent handle on halo-to-halo variance. Each merger tree traces the evolution of each of its branches back to a “leaf-mass” of $10^9 M_{\odot}$ ¹ which specifies our effective mass resolution. As we show, this is more than adequate for modeling the satellite galaxies that dominate the ASH mass budget of MW galaxies. In the following, we describe our model framework starting with the specific way we construct the ASH from the disrupted remains of satellites. Throughout, masses that refer to the main progenitor halo or galaxy are indicated with an upper-case M , while those referring to subhalos or satellites are indicated with a lower-case m .

2.2. The Accreted Stellar Halo

We refer to the final MW-sized halo at redshift $z = 0$ as the “host halo”. Halos that accrete directly onto the main progenitor of this host halo are called “first-order” subhalos, which themselves may contain subhalos that were accreted prior to merging with the main progenitor halo. We refer to such sub-subhalos as “second-order” subhalos, etc. Throughout, `SatGen` keeps track of the order of each subhalo, which, as discussed below, can change with time. Note that the accretion redshift, z_{acc} , of a halo is defined as the redshift at which it first became a subhalo, which can be very different from the redshift at which it is accreted onto the main progenitor of the host halo.

At accretion, each subhalo is assigned

- a stellar mass m_* , based on the a redshift dependent Stellar-Halo-Mass-Relation (SHMR; see Section 2.3)

¹ We have verified that pushing to a lower leaf-mass resolution of $10^8 M_{\odot}$ does not significantly change the stellar mass budget of the ASHs shown in Section 3 or in the correlations discussed in Section 4.

- an effective size r_{eff} , based on a redshift-independent empirical Size-Mass-Relation (SMR; see Section 2.4)
- a halo concentration parameter c , based on its pre-accretion MAH (see Section 2.6)
- an orbital energy and angular momentum drawn from an empirical redshift-independent probability distribution function (see Section 2.8)

The newly formed satellite system is then orbit-integrated in the potential of its direct parent halo, accounting for tidal stripping and dynamical friction, as outlined in Section 2.6. This means that all subhalos of order k are evolved in the potential of their parent halos of order $k - 1$. Any stellar mass stripped from a satellite of order k is instantaneously added to the ASH reservoir of its parent of order $k - 1$. When that parent is accreted into a bigger halo, its ASH is added to that of its new parent. In this way, all stellar mass stripped, independent of the progenitor halo in which the stripping occurred, ends up as part of the ASH of the final host halo. Note that, at any redshift z , we refer to the ASH mass as the sum of the ASH masses of *all* progenitors at that redshift. During every time step in the orbit integration any of the following can happen:

- **Disruption:** When the mass of a subhalo drops below a critical value, m_{dis} , we consider the subhalo and the satellite galaxy that it hosts to be disrupted. We define $m_{\text{dis}} = f_{\text{dis}} \times m_{\text{acc}}$, where f_{dis} is a free parameter for which we adopt the fiducial value of 10^{-4} (see Section 2.6). If a subhalo disrupts, all of its remaining stellar mass is added to the ASH of its direct parent.
- **Merging:** We assume that a satellite galaxy merges with the central galaxy of its direct parent if its orbital energy becomes too small. A fraction f_{cann} of the remaining stellar mass of the satellite is then added to the central of its direct parent, while the remaining fraction $(1 - f_{\text{cann}})$ is added to the ASH. If the satellite merges with the galaxy of the main progenitor, this fraction is also added to the $M_{\text{ex-situ}}$ component (see Sections 2.5 and 2.9). In this way we keep track of what fraction of the host galaxy's stellar mass has been accreted by cannibalizing satellites.
- **Order Dropping:** If a subhalo of order $k \geq 2$, orbits outside of the instantaneous tidal radius of its direct parent of order $k - 1$, it has a probability of being released and becoming a subhalo of order $k - 1$ (see Section 2.6). In the event of release, the phase-space coordinates of the subhalo are updated to be the superposition of its original coordinates with respect to its old parent of order $k - 1$ and its new parent of order $k - 2$. The same release mechanism is triggered if a subhalo's direct parent is found to be disrupted or merged.
- **Order Jumping:** If the direct parent of a subhalo is accreted into a bigger halo, the order of all its subhalos increase by one, i.e., $k \rightarrow k + 1$. The subhalo in question continues to be integrated with respect to the potential of its direct parent.

Unlike numerical simulations that depend on subhalo-finding algorithms and are subject to artificial overmerging, this setup with SatGen allows us to accurately track and account for the mass budgets of satellites and the ASH they produce. In the next sections we detail the different stellar mass components we consider in this work.

2.3. The Stellar Halo Mass Relation

When a halo first becomes a subhalo, we assign it a stellar mass using the redshift-dependent SHMR i.e., $m_* = m_*(m_{\text{acc}}, z_{\text{acc}})$ given by equations (J1)-(J8) of Behroozi et al. (2019). Here, m_{acc} and z_{acc} are the subhalo mass and redshift at accretion. To this mass, we add a random scatter of 0.2 dex to account for the intrinsic scatter in the SHMR. Figure 1 shows the SHMR of B19 over several decades in halo mass, and at four different redshifts, compared to similar empirical relations in the literature. For clarity we do not show the 0.2 dex scatter in stellar mass which we assume to be independent of halo mass or redshift². Note that the empirical B19 model for the SHMR predicts very little redshift evolution in the slope of the SHMR at the low mass end. However, we emphasize that the results for $m_{\text{acc}} \lesssim 10^{12} M_\odot$ are mainly extrapolations from constraints at larger masses, especially for $z > 0$, and that the SHMR at the low mass end remains poorly constrained (Allen et al. 2019; Nadler et al. 2020; Munshi et al. 2021; Santos-Santos et al. 2022; Danieli et al. 2023; O'Leary et al. 2023; Christensen et al. 2024; Monzon et al. 2024; Kado-Fong et al. 2025). Despite these uncertainties we adopt the SHMR of Behroozi et al. (2019, hereafter B19) as described above. In a forthcoming study we will test to what extent observations of stellar halos may be used to constrain the low-mass end of the SHMR (eg. Rey & Starkenburg 2022).

2.4. The Size Mass Relation

At accretion, we also assign the satellite galaxies an effective half-light radius, r_{eff} , based on the stellar-mass radius relation (SMR) inferred from the Satellites Around Galactic Analogs survey (SAGA) (Geha et al. 2017; Mao et al. 2021, 2024), which covers the stellar mass range $10^{6.75} M_\odot < m_* < 10^{10} M_\odot$, and is consistent with results in the local volume (Carlsten et al. 2022). Given a satellite's stellar mass at accretion, we draw its effective size from a log-normal distribution centered on the mean relation of Asali et al. (2025);

$$\log(r_{\text{eff}}) = 0.27 - 2.11 \log(m_*), \quad (1)$$

assuming a scatter of 0.2 dex. The slope and intercept are the best-fit values from the SAGA DR III “Gold-Sample” and we ignore the slight environmental dependence found by Asali et al. (2025). Since most of our satellites have an assigned stellar mass $m_* < 10^9 M_\odot$, we ignore any potential redshift evolution in the SMR, which is poorly constrained for such low-mass galaxies. We also emphasize that in reality galaxy sizes are correlated with other galaxy properties, such as their star formation rate and morphology. Such correlations are not taken into account in our work but we do not expect this oversimplification to significantly impact the main results of this study.

2.5. Stellar Mass of the Central Galaxy

The present-day stellar mass of the central is made up of two components; an in-situ component $M_{\text{in-situ}}$, consisting of stars that formed in the main progenitor halo, and an ex-situ component $M_{\text{ex-situ}}$, which consists of all the stars accreted by the central galaxy during satellite mergers. To build up the in-situ stellar component of the central host galaxy we follow the B19 prescription (see also Moster et al. 2018; O'Leary et al.

² We thus ignore the fact that the results of B19 are consistent with a slight increase in the scatter towards lower halo masses and higher redshifts.

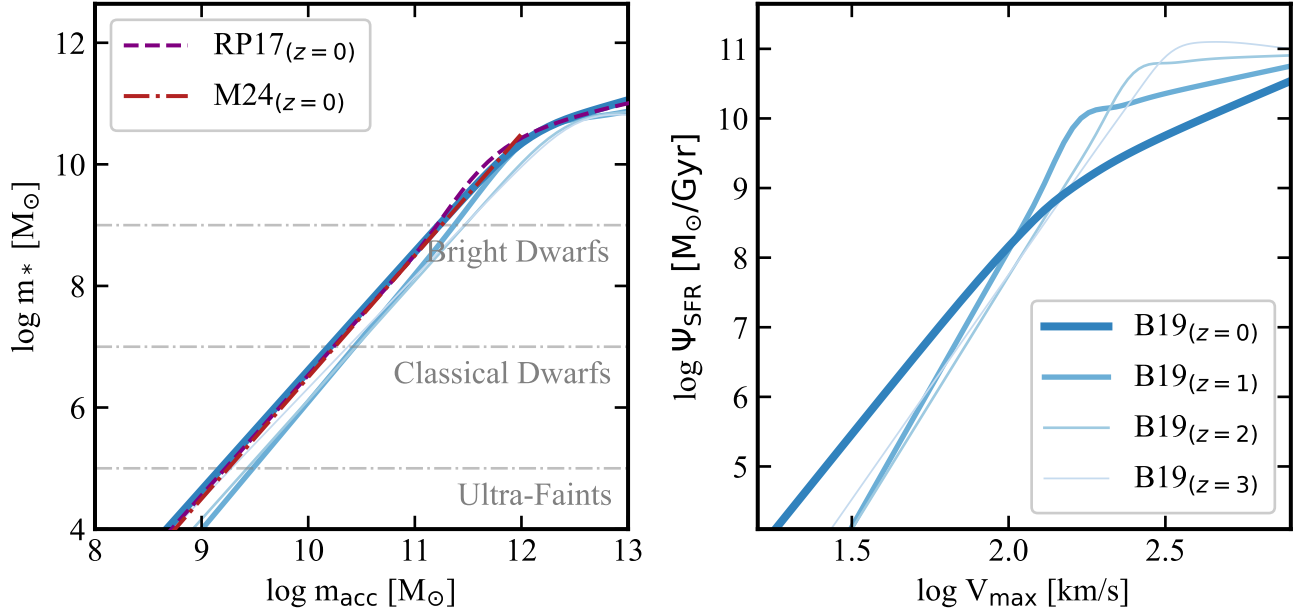


Figure 1. Left panel: The SHMR from Behroozi et al. (2019) used to assign stellar masses to all the subhalos in our merger trees at accretion. We show the relation across several decades in dark matter mass despite only populating subhalos between $10^9 M_\odot \leq m_{\text{acc}} \lesssim 10^{12} M_\odot$. For clarity we don't show the constant 0.2 dex scatter that is assumed when drawing stellar masses. For reference we show the SHMR from Rodriguez-Puebla et al. (2017) and the fiducial SHMR from Monzon et al. (2024). **Right panel:** The deterministic relation between star formation rate (SFR) and its maximum circular halo velocity V_{max} from the UniverseMachine (Behroozi et al. 2019). We use this relation to build up the “in-situ” component of central galaxies in our model by integrating SFRs across time snapshots.

2023, for similar prescriptions) and assume that a galaxy’s star formation rate ψ_{SFR} , is a function of redshift and the host halo’s instantaneous maximum circular velocity, V_{max} . The right-hand panel of Figure 1 shows the dependence of ψ_{SFR} on V_{max} at four redshifts, as indicated. Using these star formation rates (SFRs), we calculate the final in-situ stellar mass of the central galaxy according to

$$M_{\text{in-situ}} = \sum_{t_i < t} \psi_{\text{SFR}}(t_i) \Delta t_i [1 - f_{\text{return}}(t - t_i)] . \quad (2)$$

Here, the summation is over all discrete timesteps of the main progenitor’s MAH, f_{return} is the return fraction that describes the mass that is returned to the interstellar medium due to stellar evolution, and $\psi_{\text{SFR}}(t)$ is given by equations (4)–(11) of B19 assuming that $V_{\text{peak}} = V_{\text{max}}(t)$. For the return fractions, we adopt

$$f_{\text{return}}(t) = 0.05 \ln \left(1 + \frac{t}{0.0014 \text{ Gyr}} \right) , \quad (3)$$

which is taken from the Flexible Stellar Population Synthesis (FSPS) package (Conroy & Gunn 2010) assuming a Chabrier (2003) initial mass function (IMF).

Rather than simply drawing a stellar mass from a log-normal distribution centered on the SHMR, which is the method we use to assign stellar masses to our satellites at infall, this prescription automatically introduces a correlation between the stellar mass of the central of the main progenitor and its MAH. This can be seen in the right-hand panel of Figure 2 which shows a weak correlation between M_{cen} and z_{50} , defined as the redshift at which the host halo reaches 50% of its present-day dark matter mass. Note that this correlation becomes weaker in the S_{15} and S_{30} samples due to the fact that the final halo mass (M_{DM}) is a better indicator of M_{cen} than z_{50} . As shown in the left-hand panel of Figure 2, the stellar masses

of our centrals are in perfect agreement with the SHMR of B19 used to assign stellar masses to the satellites, both in terms of the normalization as well as the scatter. Hence, our method of assigning stellar masses to satellites and centrals is self-consistent.

2.6. Dark Matter Density Profiles

The fiducial SatGen model initializes all subhalos with a Navarro-Frenk-White (Navarro et al. 1997) dark matter density profile;

$$\rho_{\text{NFW}}(r) = \rho_0 \left(\frac{r}{r_s} \right)^{-1} \left[1 + \left(\frac{r}{r_s} \right) \right]^{-2} . \quad (4)$$

Here, ρ_0 is a characteristic density and $r_s = r_{\text{vir}}/c$ is the scale radius, with r_{vir} the virial radius and c the halo concentration parameter. Throughout, halo concentrations are computed using the model of Zhao et al. (2009) relating c to the average density of the Universe at the redshift at which the halo’s main progenitor reaches a mass that is 4% of its mass at accretion.

As a subhalo orbits its parent, it is exposed to tides that strip away the outer layers of its mass distribution. In SatGen this tidal stripping is modeled using the method originally pioneered by Taylor & Babul (2001) and Zentner & Bullock (2003), according to which

$$\frac{\Delta m}{\Delta t} = -\alpha_s \frac{m (> r_{\text{tid}})}{t_{\text{dyn}}} . \quad (5)$$

Here, α_s is the stripping efficiency modeled as a function of the ratio between the concentration parameters of the host and subhalo at accretion (Jiang et al. 2021; Green et al. 2021), $t_{\text{dyn}} = \sqrt{3\pi/16G\bar{\rho}(r)}$ is the dynamical time with $\bar{\rho}(r)$ the average density of the direct parent halo inside the instantaneous orbital radius r , and r_{tid} is the instantaneous tidal radius, which

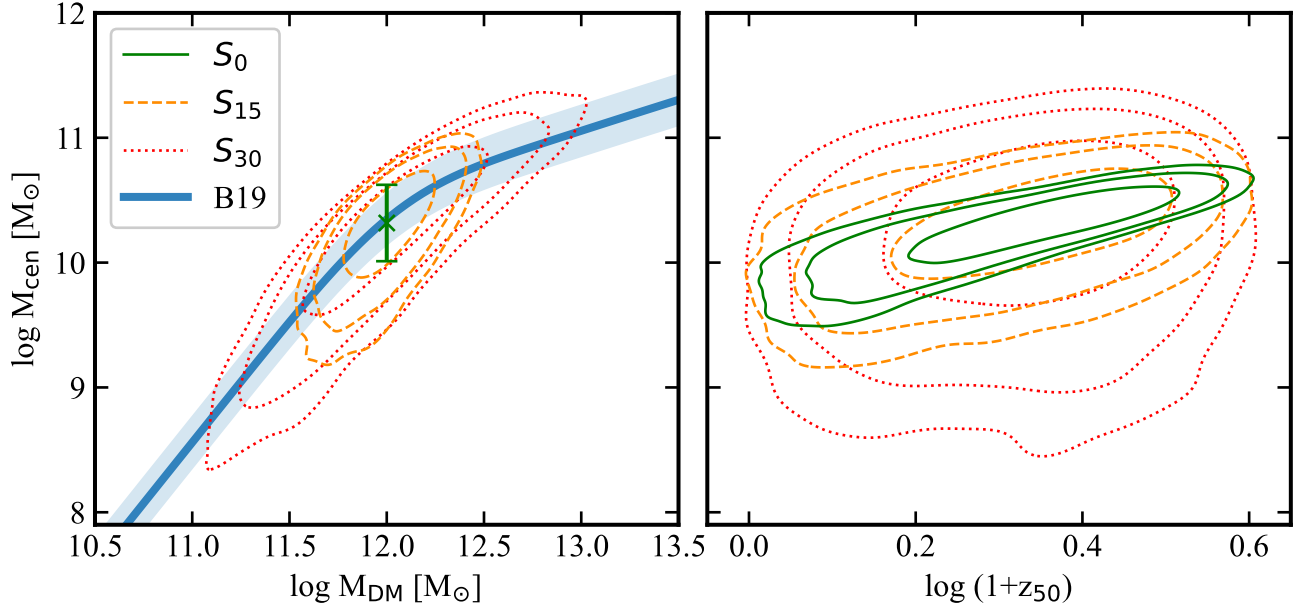


Figure 2. Left panel: The distribution of our three merger tree samples (S_0, S_{15}, S_{30}) in the SHMR plane assuming central galaxies grow according to the $\psi_{\text{SF}} - V_{\text{max}}$ relation defined in Behroozi et al. (2019). For reference we show the present-day SHMR (thick blue line) along with its 0.2 dex scatter (blue shaded region). **Right panel:** The distribution of halo formation times (z_{50}) against present-day central stellar mass. Notice how the S_0 sample spans a similar range to the other two samples despite being restricted to present-day DM mass of 10^{12} M_\odot . This illustrates what we refer to as halo-to-halo variance.

is given by the root of

$$r_{\text{tid}} = \left[\frac{Gm (< r_{\text{tid}})}{\Omega^2 - \frac{d^2\Phi}{dr^2} \Big|_r} \right]^{1/3}. \quad (6)$$

(King 1962; Tollet et al. 2017; van den Bosch et al. 2018), with Ω the subhalo’s instantaneous angular velocity and Φ the gravitational potential of the subhalo’s direct parent halo.

In order to model the density profiles of subhalo remnants that have been stripped of some of their mass, we assume that the structural properties of tidally stripped subhalos depend solely on their initial density profile and on the total amount of matter lost since accretion (Peñarrubia et al. 2008, 2010; Errani et al. 2018; Chiang et al. 2024). This means that the structural properties of subhalos evolve along “tidal tracks” and are independent of their orbit. Hence, the evolved density profile can be modeled using the initial density profile at accretion and a “transfer function” $H(r|f_b)$ that depends only on the subhalo’s instantaneous bound mass fraction $f_b \equiv m(t)/m_{\text{acc}}$. In particular, we have that

$$\rho(r, t) = H(r|f_b(t)) \rho_{\text{NFW}}(r, t_{\text{acc}}). \quad (7)$$

Throughout, we use the transfer function given by equations (5)–(8) in Green & van den Bosch (2019) that has been carefully calibrated and validated using a large suite of high-resolution idealized simulations (Ogiya et al. 2019; Green & van den Bosch 2019; Green et al. 2021).

Following Monzon et al. (2024), we assume that a subhalo (and its associated satellite galaxy) is disrupted whenever the instantaneous subhalo mass drops below a critical mass $m_{\text{dis}} \equiv f_{\text{dis}} m_{\text{acc}}$. As mentioned above, we adopt $f_{\text{dis}} = 10^{-4}$ as our fiducial value, which implies that subhalos disrupt once they have lost more than 99.99% of their initial accretion mass. We have verified that setting $f_{\text{dis}} = 10^{-3}$ or $f_{\text{dis}} = 10^{-5}$ has no significant impact on any of our results.

2.7. Evolution of Satellite Stellar Masses

In order to model the effects of tidal stripping on the satellite stellar masses, we proceed as follows. Tidal tracks analogous to those describing the tidal evolution of the dark matter properties can also be used to evolve the stellar mass (m_*) and size (r_{eff}) of an embedded satellite. Here we follow Errani et al. (2018) and assume that the ratios $m_*(t)/m_*$ and $r_{\text{eff}}(t)/r_{\text{eff}}$ follow tidal tracks characterized by

$$g(x) = \left(\frac{x_s + 1}{x_s + f_b} \right)^\mu f_b^\eta. \quad (8)$$

Here, $g(x)$ refers to either $m_*(t)/m_*$ or $r_{\text{eff}}(t)/r_{\text{eff}}$, and f_b is the instantaneous bound mass fraction of the corresponding dark matter subhalo. The additional parameters μ, η and x_s depend on the “cuspiness” of the subhalo at accretion, parameterized by the inner logarithmic slope of the subhalo’s density profile, and on the ratio $r_{\text{eff}}/r_{\text{max}}$. Here, r_{max} is the radius at which the subhalo reaches its maximum circular velocity, v_{max} , which for an unevolved NFW density profile is $\sim 2.16 r_s$. SatGen uses a simple interpolation scheme to determine the values of μ, η and x_s based on the values inferred by Errani et al. (2018) using a discrete set of simulation results that explored the relevant parameter space³

Figure 3 shows the evolution of the size (top panel) and stellar mass (bottom panel) of satellites as a function of the subhalo’s bound mass fraction, based on the model of Errani et al. (2018). Results are shown for two different values of the $r_{\text{eff}}/r_{\text{max}}$ ratio, as indicated, to illustrate how the size of a satellite affects its tidal evolution. Note that both the stellar mass and size of satellites remain largely unaffected until the subhalo has lost roughly 99% of its accretion mass. This simply reflects that the stellar body of a satellite galaxy is

³ Since those simulations modeled the stellar bodies as Plummer spheres, we are implicitly assuming the same.

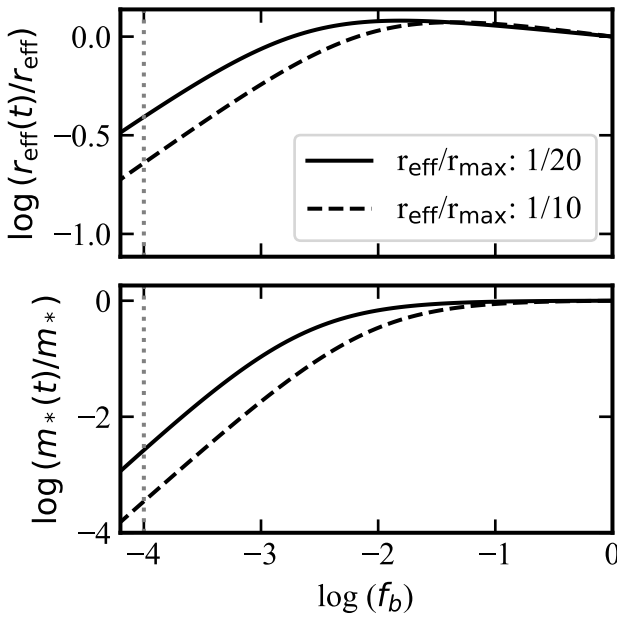


Figure 3. The stellar tidal tracks defined in Errani et al. (2018) that we use to evolve the satellites. **Top panel:** The effective radius of the satellite as a function of the bound fraction of dark matter mass (f_b). The blue lines correspond to an initially cuspy (NFW) density profile for the dark matter. The solid vs. dashed lines indicate the initial sizes of the satellite galaxies relative to their dark matter subhalos as indicated. **Bottom panel:** The stellar mass of the satellites as a function of the f_b . They grey dotted line in both panels indicates our disruption criteria. Notice that, according to these models, a significant fraction of dark matter mass must be lost before any stars can be stripped.

located near the center of the halo, where it is shielded from the tidal effects until the halo has been stripped down to the radius where the stars reside. This also explains why satellites with a larger effective radius experience more mass loss and a larger reduction in size for the same bound mass fraction of the subhalo remnant.

Any stellar mass that is stripped by tides is instantaneously deposited into the ASH. Note that we do not explicitly model the subsequent evolution of stripped stars and are therefore agnostic to where density profile of the ASH. Throughout, we make the simplifying assumption that any stellar mass lost to tides remains within the virial radius of the host galaxy and thus a part of the ASH of the final host halo.

2.8. Subhalo Orbits

Under the assumption that halos are spherical potentials, the orbital energy and angular momentum of a subhalo can be specified by two independent parameters; the infall velocity v_{inf} and the angle θ between the position and velocity vectors. For each subhalo, we initialize its orbit at accretion by randomly drawing v_{inf} and θ from their corresponding PDFs defined in Equations (1) and (2) of Li et al. (2020).

We follow the standard SatGen procedure and integrate subhalo orbits by treating them as point masses (see Jiang et al. 2021, for details). Each subhalo is integrated in the potential of its direct parent, accounting for a dynamical friction force

$$F_{\text{DF}} = -4\pi \frac{G^2 m^2}{v^2} \ln \Lambda \rho(< v) \frac{v}{|v|} \quad (9)$$

(Chandrasekhar 1943). Here, m is the instantaneous subhalo

mass, $\ln \Lambda$ is the Coulomb logarithm, v is the relative velocity of the subhalo with respect to its parent halo, and $\rho(< v)$ is the local density of dark matter particles in the parent halo with a speed less than $|v|$, which is computed under the standard assumption that the particles follow an isotropic Maxwellian velocity distribution (see Binney & Tremaine 2008). The Coulomb logarithm is modeled using

$$\ln \Lambda = \beta_{\text{DF}} \ln (M/m) , \quad (10)$$

where β_{DF} is a free parameter that regulates the overall strength of dynamical friction. As fiducial value, we set $\beta_{\text{DF}} = 1$. In Appendix A we demonstrate that increasing or decreasing β_{DF} by a factor of two only has a small impact on the final masses of the ASH and the surviving satellite population.

2.9. Mergers

Although SatGen does not allow satellites to merge with one another, they are allowed to merge with the central galaxy of their direct parent halo. Specifically, we merge a satellite galaxy with its parent if, at any point in its orbit integration, *both* its relative position (r) and speed (v) obey the following criterion

$$\log \left(\frac{r_k}{r_{\text{max},k-1}} \right) < X_{\text{merge}} \text{ AND } \log \left(\frac{v_k}{v_{\text{max},k-1}} \right) < X_{\text{merge}} . \quad (11)$$

Here, r_{max} is the radius at which the parent halo reaches its maximum circular velocity, v_{max} , and X_{merge} is a free parameter that allows us to control the frequency of central-satellite mergers.

If and when a satellite galaxy merges with its parent galaxy, we assume that a fraction f_{cann} of its instantaneous stellar mass is cannibalized by the parent. The remaining fraction is deposited into the ASH. In general, f_{cann} and X_{merge} depend on the mass ratio of the central and satellite and on the detailed orbit of the latter. Throughout, we ignore such details and instead treat both as free parameters that control the frequency of central-satellite mergers and their impact on the final masses of the ASH and the central. However, as we demonstrate in Appendix A, our qualitative results are robust to reasonable changes to both f_{cann} and X_{merge} .

Because of the possibility of mergers, the final stellar mass of the main progenitor galaxy can be written as

$$M_{\text{cen}} = M_{\text{in-situ}} + M_{\text{ex-situ}} . \quad (12)$$

where $M_{\text{in-situ}}$ is given by equation (2) and represents the stellar mass that formed in-situ due to star formation in the central galaxy of the main progenitor, while

$$M_{\text{ex-situ}} = \sum_i^{N_{\text{merged}}^{k=1}} f_{\text{cann}} m_{*,i} \quad (13)$$

is the ex-situ component due to the accretion of satellite galaxies. Note that the summation is only over first-order ($k = 1$) satellite systems, as these are the only ones that can directly merge onto the main central. As discussed in Section 2.5, the final stellar masses of our central galaxies, which include both the in-situ and ex-situ components, are consistent with the SHMR presented in B19 in terms of both the normalization and the scatter. Importantly, the ex-situ component makes a negligible contribution (typically $M_{\text{ex-situ}} < 10^{-3} M_{\text{in-situ}}$) to the stellar mass of the main central.

symbol	equation	component description
$M_{\text{in-situ}}$	(2)	stellar mass of main progenitor galaxy at $z = 0$ that formed in-situ due to star formation
$M_{\text{ex-situ}}$	(15)	stellar mass of main progenitor galaxy at $z = 0$ accreted from satellites
M_{cen}	(14)	total stellar mass of the main progenitor galaxy at $z = 0$
M_{ASH}	(16)	stellar mass of the accreted stellar halo at $z = 0$
M_{sat}	(17)	total stellar mass of surviving satellites at $z = 0$
M_{tot}	(18)	total stellar mass of all satellites at their respective z_{acc}

Table 1

Various mass components of the final halo at $z = 0$ relevant to the results presented in Section 3. The first column lists the symbol used throughout the text, the second column lists the number of the defining equation, and the third column gives a brief description.

Similarly, we can write the final mass of the ASH as a sum over three contributions

$$M_{\text{ASH}} = \sum_{i=1}^{N_{\text{surviving}}} m_{*,i}^{\text{lost}} + \sum_{i=1}^{N_{\text{disrupt}}} m_{*,i} + \sum_{i=1}^{N_{\text{merged}}} (m_{*,i}^{\text{lost}} + m_{*,i}^{\text{deposit}}). \quad (14)$$

The first sum is over all surviving satellite galaxies, where $m_{*,i}^{\text{lost}}$ is the total stellar mass that the satellite has lost to tidal stripping since its accretion. The second sum is over all satellites that have been completely disrupted and therefore contribute their entire stellar mass budget to the ASH. The third and final sum is over all satellites that have merged with their parents. Each of these contribute the sum of $m_{*,i}^{\text{lost}}$ plus $m_{*,i}^{\text{deposit}}$ to the ASH. The former is the stellar mass lost to tidal stripping prior to merging with the parent, while

$$m_{*,i}^{\text{deposit}} = (1 - f_{\text{cann}}) (m_{*,i} - m_{*,i}^{\text{lost}}) \quad (15)$$

is the stellar mass of the satellite that is deposited into the ASH as a consequence of the merger.

At $z = 0$, the sum of all stellar masses assigned to satellite galaxies at accretion is made up of three components

$$M_{\text{tot}} = M_{\text{ex-situ}} + M_{\text{ASH}} + M_{\text{sat}} \quad (16)$$

Here, M_{sat} is the total stellar mass of the surviving satellites, which is given by

$$M_{\text{sat}} = \sum_{i=1}^{N_{\text{surviving}}} (m_{*,i} - m_{*,i}^{\text{lost}}). \quad (17)$$

Note that, depending on its orbit and final fate, a satellite can at most contribute to two of these three mass components. For convenience, Table 1 lists the various masses that are relevant to the results in Section 3 below. Finally, we caution against assigning too much value to the distinction between merged and disrupted systems. Whether a satellite merges with its parent or experiences complete disruption is sensitive to the specific merger and disruption criteria adopted, which are somewhat ad hoc. In both cases, the satellite ends up depositing most of its stellar mass to the ASH. Hence, whether the satellite disrupts or merges has little to no impact on any of our main results.

3. RESULTS

We now use the model described above to examine how the ASH of a MW-like galaxy builds up over time. After presenting predictions for our fiducial model, we demonstrate the important role played by a handful of the most massive progenitors and discuss the impact of various sources of stochasticity.

3.1. Fiducial Model

The merger trees and the treatment of the tidal evolution of dark matter subhalos in `SatGen` have been carefully calibrated and tested in a number of previous studies (van den Bosch & Jiang 2016; Jiang & van den Bosch 2017; Green & van den Bosch 2019; Jiang et al. 2021; Green et al. 2021; Monzon et al. 2024). The specific implementation used here, and described above, has a number of additional ingredients that are not standard for the `SatGen` model. These include the assignment of stellar masses and sizes at accretion, discussed in Sections 2.3 and 2.4, respectively, and three free parameters related to the treatment of mergers. These are the parameter β_{DF} that controls the strength of dynamical friction (see equation [10]), the parameter X_{merge} that specifies the merger criterion (equation [11]), and the parameter f_{cann} that characterizes the fraction of stellar mass of the satellite that is cannibalized by the parent galaxy during a merger (equation [13]). As shown in Appendix A, the three main mass components of interest, M_{cen} , M_{ASH} and M_{sat} , are relatively insensitive to our choice of free parameters. In what follows, we therefore adopt the following fiducial values; $\beta_{\text{DF}} = 1$, $X_{\text{merge}} = -2.0$ and $f_{\text{cann}} = 0.8$.

Figure 4 shows the resulting stellar mass distributions of the central galaxy (left panel), the ASH (middle panel), and the combined stellar mass of all surviving satellites (right panel) for this fiducial model. Each color shows the PDFs obtained from the 10,000 unique merger trees in each of the three merger tree samples, as indicated. Typically, the stellar mass of the central galaxy is at least an order of magnitude larger than that of the ASH, which in turn is about an order of magnitude larger than that of the surviving satellite population. Note the large variance in the M_{ASH} and M_{sat} distributions which, as expected, increases with the inclusion of host halo mass-mixing (i.e., going from sample S_0 to S_{30}).

3.2. Satellite Survival

On average, $\sim 66\%$ of all satellites in our fiducial model are classified as merged or disrupted and are responsible for $\sim 95\%$ of the final mass of the ASH.⁴ This is broadly consistent with the AURIGA simulations (Shipp et al. 2024), which show that the majority of all accreted satellites around MW-like hosts have been disrupted. The remaining $\sim 34\%$ of all satellites that survive to the present-day only end up contributing $\sim 5\%$ to the present-day ASH. This is a direct consequence of the fact that the stellar components of satellites are shielded by their dark matter halos, such that a satellite only starts to experience significant stellar mass loss after its subhalo has lost $\sim 99\%$ of its initial mass (see Figure 3). Hence, most of the surviving satellites are still largely intact, with stellar

⁴ Most of this comes from the stellar mass lost to tides prior to the merger, rather than mass that is deposited into the ASH during the merger event itself.

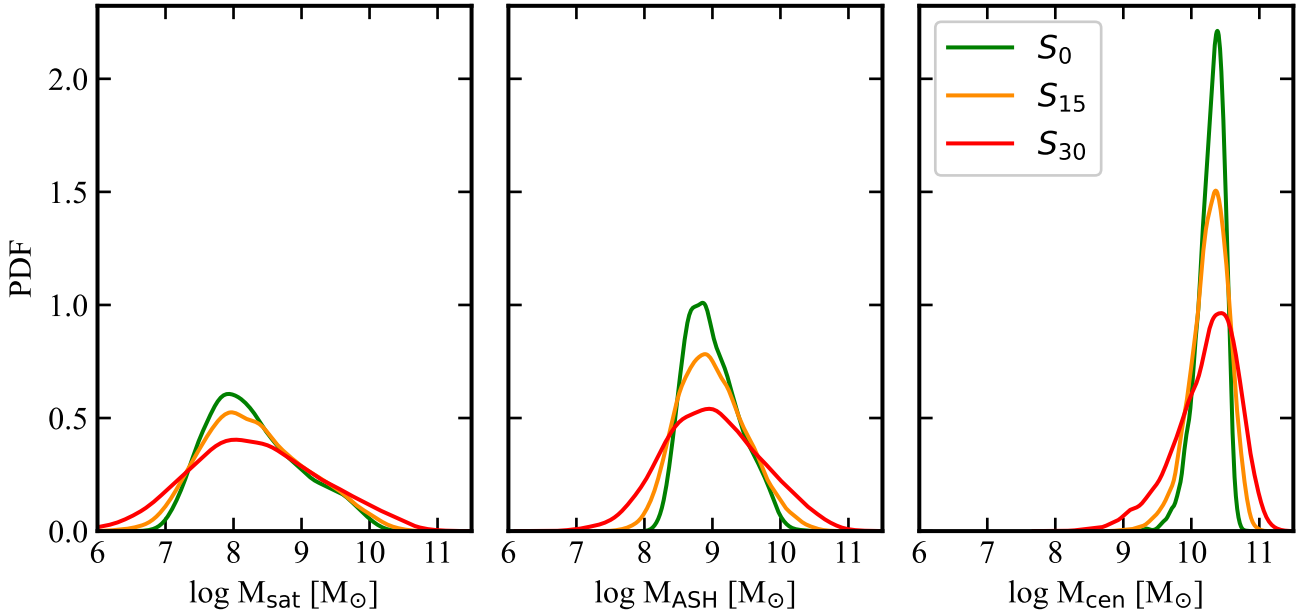


Figure 4. The fiducial distributions of the main mass components in our model for all three merger tree samples: S_0 , S_{15} , S_{30} . **Left panel:** shows the PDFs of the M_{sat} component which are all centered on $\sim 10^8 M_{\odot}$. **Middle panel:** the PDFs of the M_{ASH} component which are all centered on $\sim 10^9 M_{\odot}$. **Right panel:** shows the PDFs of the M_{cen} component which are all centered on $\sim 10^{10} M_{\odot}$. Notice that all distributions widen as the amount of host halo mass-mixing increases.

masses comparable to those at accretion. In fact, for the S_0 sample, we find that 84% of all surviving satellites have a present-day stellar mass that is larger than 0.78 of their stellar mass at accretion.

N -body simulations and semi-analytic models predict that satellite survival depends strongly on satellite mass, accretion epoch, and host galaxy structure (Bullock et al. 2001; Taffoni et al. 2003; Bullock & Johnston 2005). Several studies have examined the statistics of satellite (or subhalo) survival in MW-like host halos (e.g. Diemand et al. 2007; Geen et al. 2013; Joshi et al. 2024; Grimozi et al. 2024; Joshi et al. 2025; Pathak et al. 2025). Unfortunately, these studies are all based on numerical simulations of at most a handful of MW-like systems, and thus subject to relatively poor statistics. In addition, it is well known that simulations suffer from artificial disruption and issues with consistently tracking subhalos or satellites across different outputs. With the model presented here, we are in a unique position to study the statistics of satellite survival in MW-like hosts, unimpeded by numerical issues.

Using the 10,000 host galaxies in the S_0 merger tree sample, we select every subhalo that was accreted onto the main progenitor as a first-order⁵ subhalo and with an associated stellar mass above $10^5 M_{\odot}$ (roughly our completeness limit). For each, we register the stellar mass at accretion, m_* , the redshift of accretion onto the main progenitor, z_{acc} , and whether the satellite survives to the present-day or not. The top panel of Figure 5 indicates the survival probability (P_{survival}) of satellites, as a function of m_* and z_{acc} , measured using a simple 15 x 15 binning scheme. Here, the lighter yellow cells denote higher probabilities of survival as indicated. Figure 5 clearly shows that satellites accreted at redshifts $z > 3$ only have a small probability of surviving to the present (see also Geen et al. 2013), and only if they are low mass ($m_* \lesssim 10^7 M_{\odot}$). More specifically, the accretion redshift above which the survival probability is less than 50% decreases from $z_{\text{acc}} = 2.89$ for satellites with $m_* \sim 10^5 M_{\odot}$, to $z_{\text{acc}} = 0.70$ for $m_* \sim 10^7$, to $z_{\text{acc}} = 0.32$ for $m_* \sim 10^9 M_{\odot}$. The fact that P_{survival} decreases with increasing stellar mass is due to the fact that more massive satellites experience stronger dynamical friction, but also to the fact that more massive satellites are accreted at lower redshift which is evident from the absence of data in the upper-right corner of the panel.

The bottom panel of Figure 5 shows the median accretion redshift of satellites as a function of their stellar mass at accretion and the error bars indicate the corresponding 16-84 percentile ranges. Yellow and blue symbols denote surviving and disrupted/merged satellites, respectively. Two trends are noteworthy; more massive satellites are accreted later (independent of whether they survive to the present or not) and at fixed stellar mass, a satellite’s accretion redshift is the primary determinant of its survivability. In fact, the probability that *any* surviving satellite was accreted prior to $z = 1.0$ ($z = 3.0$) is 0.45 (0.06). Among the surviving systems, more massive satellites have been accreted more recently. We measure the median accretion redshift for the most-massive surviving satellite across the S_0 sample as $z_{\text{acc}} = 0.36$ with a 16-84 percentile range of $0.11 < z_{\text{acc}} < 0.89$.

Finally, for every system that does not survive, we also compute the time interval between disruption and infall (Δt_{dis}). When selecting satellites that lie above the “classical” dwarf galaxy regime ($m_* > 10^7 M_{\odot}$), we measure a median disruption timescale of 4.20 Gyr with a wide 16-84 percentile range of 1.08 - 7.56 Gyr. This is remarkably consistent with the range of timescales reported in simulation-based analyses (Grimozi et al. 2024; Pathak et al. 2025; Joshi et al. 2025).

⁵ To facilitate a comparison with simulation results, we restrict our analysis to first-order ($k = 1$) subhalos of the main progenitor.

3.3. Dominant Progenitors

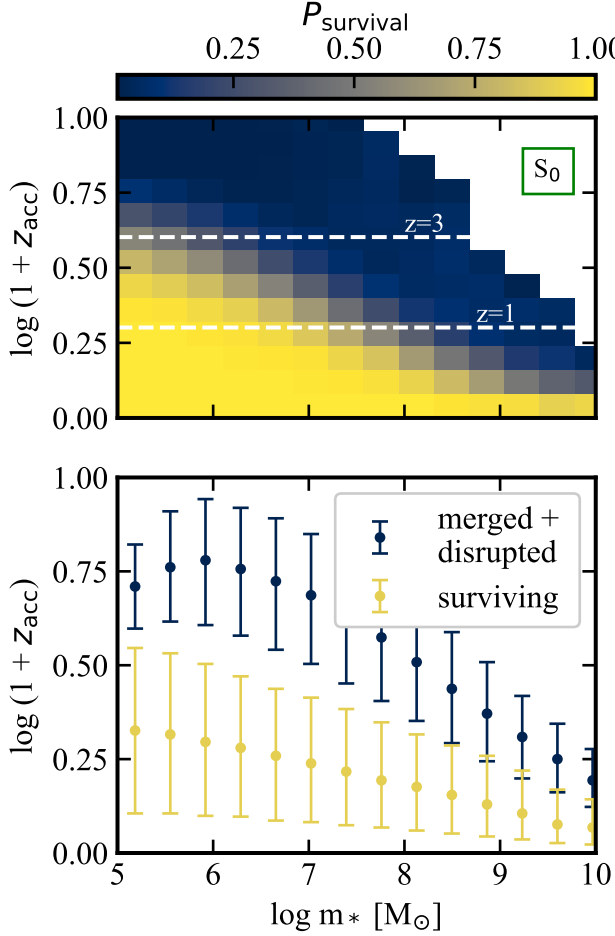


Figure 5. Top Panel: The stellar masses (m^*) at accretion vs accretion redshift (z_{acc}) for all 1st order satellites in the S_0 sample. The grid indicates a simple 15×15 binning scheme in which survival probabilities were measured. Here, the lighter yellow cells denote higher probabilities of survival as indicated. Notice that, for a fixed z_{acc} , increasing stellar mass coincides with lower survival probability. **Bottom Panel:** The distribution of accretion redshifts binned by stellar mass. Here each point marks the median and 16-84 percentile, and the color indicates the satellite population. This clearly shows that for a fixed stellar mass, systems that survive are those which were accreted more recently.

Previous studies based on simulations have shown that the ASHs of MW-like galaxies are predominantly built up from only a handful of the most massive accreted satellites (Bullock & Johnston 2005; Cooper et al. 2010; Deason et al. 2016; Fattahi et al. 2019; Monachesi et al. 2019; Orkney et al. 2022; Khoperskov et al. 2023; Pu et al. 2025). In this section we examine which progenitors contribute the most to the ASH in our model using two summary statistics; the stellar mass at accretion of the most massive⁶ progenitor (M_*^{MMP}), and the number of mass-ranked progenitors responsible for 90% of the present-day ASH mass (N_{90}).

Figure 6 shows scatter plots of M_{ASH} as a function of M_*^{MMP} . Here every point represents a host galaxy from the S_0 sample color-coded based on the accretion redshift of its most massive progenitor. For clarity, we forgo showing results for the S_{15} and S_{30} samples, but they are qualitatively the same. Surviving satellites are shown in the top panel, and merged or disrupted satellites in the bottom panel.

⁶ Here “most massive” refers to the stellar rather than the dark matter mass.

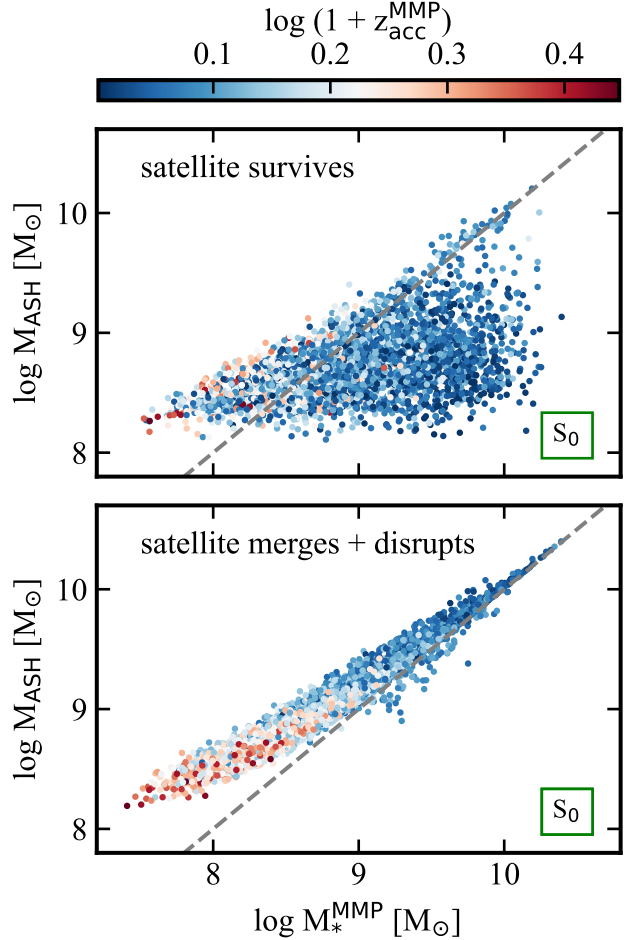


Figure 6. A scatter plot of the stellar mass at accretion of the massive progenitor satellite vs. the accreted stellar halo mass M_{ASH} in S_0 sample. The points are colored by the accretion redshift of the satellite z_{acc} . **Top panel:** The host halos whose most massive progenitor survives to present-day. **Bottom panel:** The host halos whose most massive progenitor merges or disrupts. The merged+disrupted populations sit clustered near the one-to-one line because if the most massive progenitor does not survive as a satellite, its remains dominate the M_{ASH} . The surviving population covers the same parameter space but extends to the bottom right of the panel where galaxies have low M_{ASH} but high M_*^{MMP} . This figure illustrates that a single satellite can significantly alter the stellar mass budget in M_{ASH} component.

The bottom panel of Figure 6 shows that if the most massive progenitor disrupts or merges, it typically contributes a very substantial fraction of the total mass of the ASH. The slight deviation away from the one-to-one relation (grey-dashed line) at lower masses is simply due to the fact that more than just the most massive progenitor can deposit stars into the ASH. Since massive progenitors typically experience significant dynamical friction, a large fraction of the most massive progenitors sink to the center of their host where they either merge with their parent galaxy or experience complete disruption due to the strong tides. Indeed, only $\sim 31\%$ of the most massive progenitors in the S_0 sample survive to the present-day. Interestingly, this is comparable to the survival fraction of the entire satellite population (34%), which seems at odds with the fact that more massive satellites experience stronger dynamical friction. The reason is that the most massive progenitor is typically accreted relatively late compared to the average satellite as seen by the lack of a clear color gradient in the

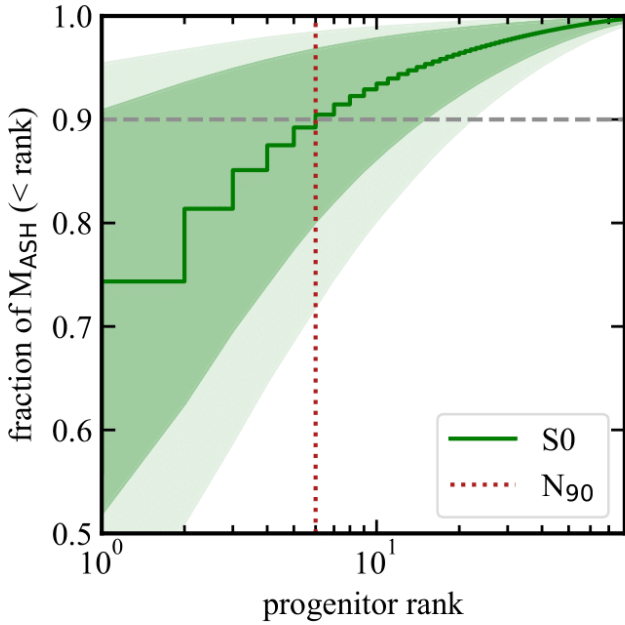


Figure 7. The cumulative distribution of the present-day ASHs as function of progenitor rank from the S_0 sample. The solid green line shows the median value across each progenitor rank and the shaded regions show the 16-84 (darker shade) and 5-95 (lighter shade) percentiles across the sample. The grey dashed line indicates 90% of the present-day M_{ASH} which we take define the number of significant progenitors N_{90} . The maroon dotted line indicates the median value of $N_{90} = 6$.

surviving population.

If the most massive progenitor survives to the present-day, either because it was accreted recently or because it ended up on a more circular orbit along which the tides are weaker, its contribution to the ASH is typically much smaller. In fact, the lack of points well above the one-to-one line at the massive end indicates that massive ASHs in MW-like galaxies are primarily built through the accretion and eventual disruption of their most massive progenitor satellites (Deason et al. 2016). Altogether, these results emphasize how the final fate of a single massive satellite can have a significant effect on M_{ASH} .

Next we rank-order the progenitors by the amount of stars they contribute to the ASH. Note that the highest ranked progenitors are not necessarily the most massive. Instead, highly-ranked progenitors are preferentially those that were assigned more eccentric orbits which results in smaller peri-centric distances and therefore in more tidal mass loss. Figure 7 shows the cumulative distribution of the M_{ASH} component as a function of these mass-ranked progenitors. Since the results are virtually identical across all three merger tree samples, we only show results for the S_0 sample. The solid green line shows the median value for the entire sample, while the shaded regions show the 16-84 and 5-95 percentiles. Using the same formalism as in Monachesi et al. (2019), we calculate the number N_{90} of mass-ranked progenitors that, when combined, are responsible for at least 90% of the final ASH mass. The dotted red line in Figure 7 shows the median value of N_{90} which, for our fiducial S_0 model, is 6 progenitors. This is in excellent agreement with Monachesi et al. (2019) who reported a median value of $N_{90} \approx 6.5$ based on the Auriga suite of 30 MW-like galaxies. Importantly, we measure the 16-84 percentile range to be 1 to 11, which is also consistent with Monachesi et al.

(2019) who report N_{90} ranging from 1 to 14.

3.4. Sources of Stochasticity

The semi-analytical framework of SatGen allows for a straightforward investigation of the various sources of stochasticity that ultimately give rise to the large variance in M_{ASH} . The main sources of stochasticity are (i) the variance in mass accretion histories of the host halo, (ii) the random orbit that is assigned to each satellite galaxy at accretion, (iii) the assumed scatter in the empirical relations used to assign satellite sizes and stellar masses at accretion, and (iv) the variance in host halo masses (in samples S_{15} and S_{30}). Except for a weak correlation between host halo mass and assembly history (more massive halos assemble later, see e.g., van den Bosch 2002), these four sources of stochasticity are independent of each other.

In order to quantify how each of these sources of stochasticity impact the ASH, we select a single merger tree whose M_{ASH} lies near the median of the S_0 sample. We use this merger tree to construct 1,000 realizations of the stellar halo, each time assigning the satellites different orbits at accretion, but keeping the same stellar masses and sizes. Hence, each realization yields a different M_{ASH} , whose variance is due solely to the stochasticity associated with the assignment of satellite orbits. The blue dotted curve in Figure 8 shows the resulting PDF for M_{ASH} . The pronounced double peak is yet another manifestation of the prominent role played by the most massive progenitor; the left peak corresponds to orbital draws for which the most massive progenitor survives to the present-day, thus contributing little to the ASH, while the right peak corresponds to orbital draws that result in either complete disruption or merging of the most massive progenitor. The vertical blue dotted line in the inset shows that orbital stochasticity alone contributes a little more than 0.2 dex to the scatter in the final M_{ASH} .

Next, we repeat the same exercise except that this time, in addition to resampling the orbits, we also resample the stellar masses and sizes at accretion. Hence, we add the impact of stochasticity resulting from the scatter in the SHMR. The corresponding results are shown as the blue dash-dotted curve. Although the two peaks of the PDF have both broadened somewhat, the PDF is still clearly bimodal. The inset shows that the overall variance in M_{ASH} has barely increased. Hence, the impact of orbit stochasticity dominates that of scatter in the assumed empirical relations.

The solid green line shows the PDF for M_{ASH} for the entire S_0 sample (identical to the middle panel in Figure 4), which displays the combined impact of stochasticity due to orbit initialization, scatter in the SHMR, and halo-to-halo variance in MAHs. As is apparent from the inset, the added stochasticity due to the latter significantly boosts the scatter in M_{ASH} to ~ 0.4 dex. The main reason is that, as demonstrated in Section 3.3 above, the ASH is dominated by the contribution of only a handful of satellites. Hence, M_{ASH} is susceptible to discreteness noise originating from variance in the masses and accretion redshifts of the most massive progenitor halos. Note that this relative impact of the massive progenitors is amplified by the steep slope of the SHMR at the low mass end, which ensures that massive progenitors contribute a stellar mass that is disproportionately high. Hence, it is expected that the level of stochasticity contributed by the halo-to-halo variance of MAHs is larger (smaller) when the low-mass slope of the SHMR is steeper (shallower). See Section 4.1 below for more detailed discussion.

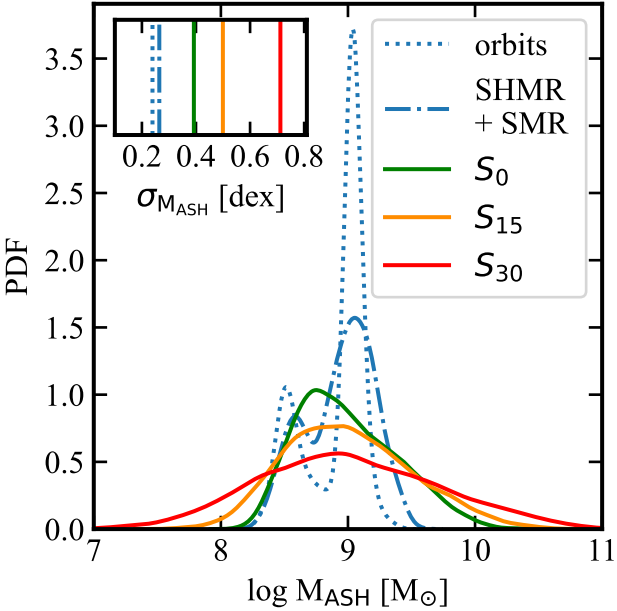


Figure 8. The PDFs of M_{ASH} across the different stochasticity models discussed in Section 3.4. Here the blue lines correspond to a single merger tree realization while the green, orange and red lines correspond to the S_0 , S_{15} and S_{30} merger tree samples, respectively. The small inset panel on the top left shows the standard deviation across the samples. Following the legend from top to bottom, the blue dotted curve is a model that only includes stochasticity from orbit initialization, the blue dash-dotted curve adds in stochasticity from assumed scatter in the empirical assignment of stellar mass and size, the green curve adds in the stochasticity from halo-to-halo variance, and finally the orange and red lines add in stochasticity from host halo mass-mixing.

Finally, the orange and red curves in Figure 8 show the effects of including host halo mass-mixing. As expected, this significantly increases the variance in M_{ASH} and ends up being the dominant source of stochasticity simply because more (less) massive host halos accrete more (less) massive substructure. Comparing the PDFs for the S_{15} and S_{30} samples, it is evident that the additional 0.15 dex increase in the scatter of the host halo mass translates to ~ 0.2 dex increase in the scatter of M_{ASH} .

3.5. Example Mass Accretion Histories

The above analysis shows that variance in MAHs translates into variance in M_{ASH} . One of the main goals of this work is to investigate to what extent these properties are correlated. To build some insight, we select 4 merger trees from the S_0 sample with different formation times that roughly sample the full range of z_{50} . The corresponding MAHs are shown in the top panel of Figure 9, where each small step in an individual MAH represents a subhalo that was accreted onto the main progenitor at that time. For ease of reference, in what follows we refer to these MAHs as *earliest* ($z_{50} = 1.85$), *early* ($z_{50} = 1.17$), *late* ($z_{50} = 0.43$) and *latest* ($z_{50} = 0.11$).

The middle panel shows the growth histories of the central galaxies. The fact that these four halos have unique MAHs results in four distinct central stellar masses despite having identical host halo masses (see Section 2.5). Notice the relative smoothness in the growth of the stellar mass of the central component compared to the step-like increase of the mass of the dark matter halo. This is a consequence of the fact that the build-up of stellar mass involves an integration of the star formation rate across cosmic time, buffered by a time-

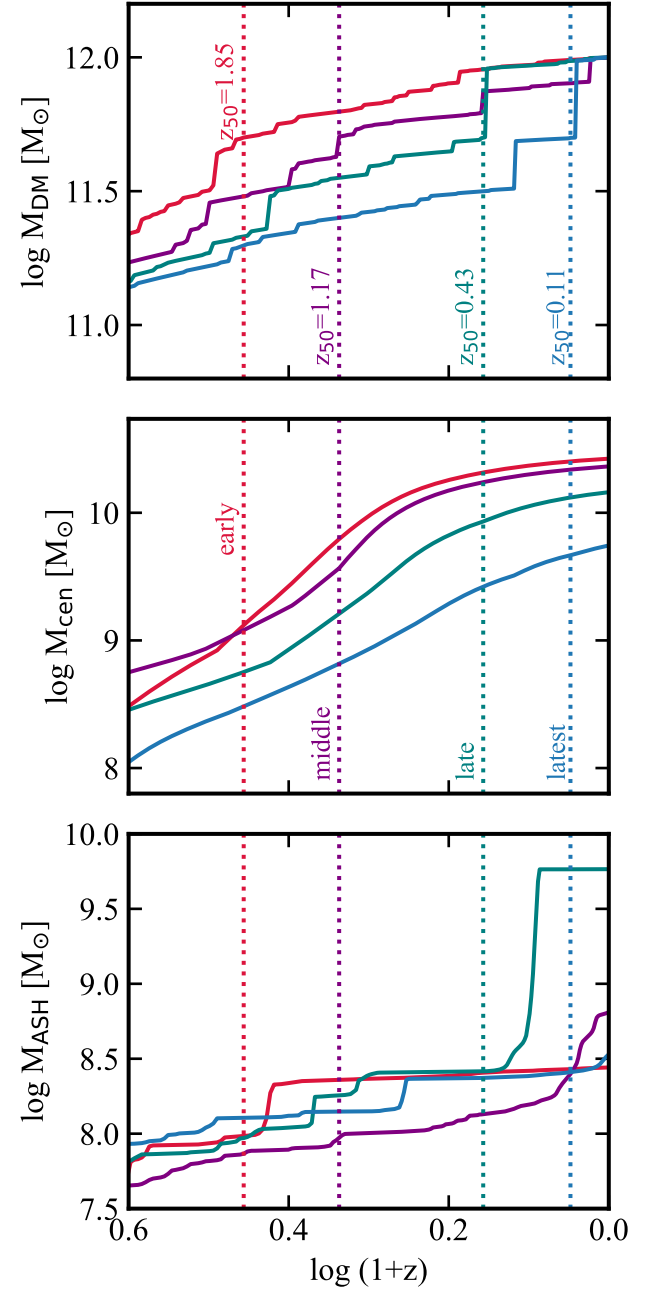


Figure 9. The MAHs of the four illustrative example galaxies described in Section 3.4. **Top panel:** The dark matter MAHs and corresponding z_{50} values. There is significant variance across the four examples despite them all having the same present-day mass of $M_{\text{DM}} = 10^{12} M_{\odot}$. **Second panel:** The central galaxy MAHs whose shape is dominated by the $M_{\text{in-situ}}$ component. Notice that the earliest forming galaxy has the largest M_{cen} by $z = 0$. **Third panel:** The stellar halo MAHs whose shapes are a convolution of the dark matter MAHs and the subsequent satellite orbit evolution.

dependent return fraction (see Section 2.5). At $z = 0$, there is a clear positive correlation between M_{cen} and z_{50} , with the halos that assemble earlier hosting a more massive central galaxy (see also Figure 1). This correlation is a consequence of the enhanced SFRs at early times in the in-situ model that dominates the M_{cen} component.

Finally, the bottom panel shows the evolution of the ASH mass. Notice the step-like cadence similar to that in the top-most panel. This simply reflects that the ASH builds up it

mass from the accretion and subsequent stripping of individual satellite galaxies (see also Figure 8 of [Cooper et al. \(2010\)](#)). Despite this correspondence between the assembly history of the host halo and that of its ASH, it is clear that the final ASH mass is poorly correlated with host halo formation time. In particular, the most massive ASH has formed in the *late* host, which has an intermediate formation time, whereas the *early* and *latest* hosts have ASH masses that are extremely similar, despite having halo formation times that are very different. The main reason for this weak correlation is the impact of the other sources of stochasticity, in particular that arising from the random orbits assigned to the satellites. For example, the *latest* tree accretes its most massive progenitor ($m_{\text{acc}} = 10^{11.67} \text{ M}_\odot$) at $z = 0.11$ which is initialized with an orbit that neither merges with the central galaxy nor disrupts by $z = 0$. In contrast, when the *late* tree accretes its most massive ($m_{\text{acc}} = 10^{11.60} \text{ M}_\odot$) progenitor at $z = 0.43$, it is initialized with an orbit that sees it merge with the central in less than ~ 2 Gyrs. Dynamical friction, tidal stripping and the eventual merger event transfer almost the entirety of its $10^{9.74} \text{ M}_\odot$ stellar budget to the M_{ASH} component. This large deposit of stars is evident as the sharp jump in M_{ASH} for the *late* system at $z \sim 0.09$, roughly 2 Gyrs after the satellite system was accreted.

These four examples demonstrate that the stellar mass of both the central galaxy and the ASH depend strongly on the MAH of the host halo, even at fixed present-day halo mass. However, other stochastic elements, in particular the orbital parameters of the accreted satellites, also strongly impact the buildup of the stellar halo, thereby reducing the correlation between M_{ASH} and the system’s assembly history. Whether or not the correlation remains strong enough to put meaningful constraints on a galaxy’s MAH from measurements of its ASH is the topic of the next section.

4. INFERRING GALAXY ASSEMBLY HISTORIES

In this section, we quantify how a galaxy’s mass accretion history (MAH) is encoded in its present-day halo observables. To do so, we assume that the following mass components are, in principle, observable for every galaxy: the stellar mass of the central galaxy (M_{cen}), the accreted stellar mass in the halo (M_{ASH}), and the cumulative stellar mass of all surviving satellites (M_{sat}). We refer to this set of observables, $[M_{\text{cen}}, M_{\text{ASH}}, M_{\text{sat}}]$, as the “input features”. From these inputs, we aim to infer three distinct “target variables” that characterize the galaxy’s MAH: (i) the redshift at which the host halo assembled 50% of its present-day mass (z_{50}); (ii) the number of progenitor galaxies contributing 90% of the present-day stellar halo (N_{90}); and (iii) the dark matter mass of the most massive progenitor halo ($M_{\text{acc}}^{\text{MMP}}$) at accretion.

We first measure the Spearman rank-order correlation coefficients (ρ_S) in each merger tree sample for each pair of input feature and target variable. The resulting measurements are listed in Table 2. Notice how, for almost each target variable, the inclusion of host halo mass-mixing decreases the correlation strength as measured by $|\rho_S|$ (See Appendix B for a more detailed discussion of these correlation coefficients and their physical interpretations). Below we quantify how each input feature correlates with different definitions of halo formation time and we train a Random Forest Regression algorithm (RFRa) on subsets of our merger tree samples to see how well they recover truth values in our target variables.

4.1. Correlation Strengths

sample	S_0	S_{15}	S_{30}
$\rho_S (M_{\text{cen}})$			
z_{50}	0.852	0.528	0.225
N_{90}	0.452	0.262	0.139
$M_{\text{acc}}^{\text{MMP}}$	-0.648	0.006	0.525
$\rho_S (M_{\text{ASH}})$			
z_{50}	-0.538	-0.458	-0.422
N_{90}	-0.965	-0.785	-0.567
$M_{\text{acc}}^{\text{MMP}}$	0.669	0.771	0.884
$\rho_S (M_{\text{sat}})$			
z_{50}	-0.342	-0.352	-0.365
N_{90}	0.257	0.219	0.134
$M_{\text{acc}}^{\text{MMP}}$	0.090	0.327	0.611

Table 2
The Spearman rank-order correlation coefficients between the input features and target variables. Each measurement is made across the 10,000 galaxies in each merger tree sample (separated by columns). See Figure 16 for the accompanying 2D contour plots.

It is common to quantify the halo formation (or assembly) time by z_{50} , the redshift at which the main progenitor has assembled 50% of its final mass. However, this is fairly ambiguous and it might well be that other epochs in a halo’s formation history are more strongly correlated with the final properties of the halo’s stellar content. Our `SatGen` model is ideally suited to examine this in detail. For each of our three input features (M_{cen} , M_{ASH} , and M_{sat}) and for each of our three samples (S_0 , S_{15} and S_{30}) we compute the Spearman rank-order correlation coefficient between the input feature and the halo formation redshift z_f , defined as the redshift at which the main progenitor has assembled a fraction f of the final $z = 0$ halo mass. We do this for a range of different values of f , ranging from 0.01 to 0.99 in steps of 0.01.

The results are shown in Figure 10, which shows ρ_S as a function of f . Different panels correspond to different input features, while different colors correspond to different halo samples, as indicated. Note that whereas M_{cen} is positively correlated with z_f , both M_{ASH} and M_{sat} are anti-correlated with halo formation time. The positive correlation between M_{cen} and halo formation time is an outcome of the fact that star formation is more efficient at higher redshifts, such that halos that assemble earlier, build up a larger stellar mass (see Section 2.5). The anti-correlations between M_{ASH} , M_{sat} , and z_f arise from the assumed SHMR. Hierarchical structure formation dictates that numerous low-mass progenitors dominate accretion onto host galaxies at early times while more massive progenitors are typically accreted at later times. If the slope at the low-mass end of the SHMR is steeper than unity (i.e. $d \log m_*/d \log M_{\text{DM}} > 1$), more massive progenitors bring in a stellar mass that is disproportionately high. As a consequence, host galaxies that assemble a large fraction of their mass at late times, through the accretion and (potential) disruption of a handful of massive satellites, will naturally exhibit larger M_{ASH} and M_{sat} ([Cooper et al. 2013](#); [Amorisco 2017](#); [Elias et al. 2018](#); [Rey & Starkenburg 2022](#)). Hence, the anti-correlations with z_{50} seen in the lower two panels of Figure 10, arise from the fact that our assumed SHMR has a slope of $d \log m_*/d \log M_{\text{DM}} \simeq 2$ below $M_{\text{DM}} \sim 10^{12} \text{ M}_\odot$.

This has an interesting corollary. The slope of the SHMR is known to change from greater than unity to less than unity around a halo mass of $\sim 10^{12} \text{ M}_\odot$ (e.g., [Moster et al.](#)

2010; Yang et al. 2012; Behroozi et al. 2019). Hence, halos with a mass less than (or comparable to) that of the MW will typically accrete subhalos that fall in the range where $d \log m_*/d \log M_{\text{DM}} > 1$, thus giving rise to an anti-correlation. However, halos with $M \gtrsim 10^{13} M_{\odot}$ are expected to accrete most of their mass from progenitors that fall in the range where $d \log m_*/d \log M_{\text{DM}} < 1$. Consequently, we expect their M_{ASH} and M_{sat} to be positively correlated with the halo formation time. We investigate this in more detail in a forthcoming study (Monzon et al. in prep).

As is evident from Figure 10, each of the three input features reveals a different dependence on f . In particular, while M_{cen} is most strongly correlated with halo assembly time for $f = 0.5$, M_{sat} and M_{ASH} reveal their strongest correlation for $f \sim 0.85$ and $f \sim 0.45$, respectively. This indicates that the total mass in surviving satellites is a good indicator of the halo's more recent assembly history, while the stellar mass of the central and its ASH are more indicative of the host halo's earlier assembly history. These trends are easy to understand. The stellar mass of the central and its ASH built up over the entire assembly history. In particular, the star formation rate of the central galaxy closely follows the assembly history of the main progenitor (see Section 2.5) while the final ASH is the aggregate of stars stripped from satellites in all progenitors (see Section 2.9). In the case of satellite galaxies, the situation is different since the vast majority either completely disrupt, merge with the central, or lose a substantial fraction of their mass to the ASH. Because of this, only satellites that were accreted relatively recently make a significant contribution to the final stellar mass of surviving satellites, which explains why M_{sat} is a good gauge of the halo's recent accretion history (see Section 3.2 for further discussion).

Comparing the results for our three different halo samples, it is clear that host halo mass-mixing drastically suppresses the correlation between halo formation time and central stellar mass. This is basically a consequence of the fact that more massive halos typically form more massive centrals, which implies a positive correlation between halo mass and M_{cen} . Since more massive halos assemble later, this implies a negative correlation between z_f and M_{cen} . However, at fixed halo mass, the results for the S_0 sample clearly reveal a positive correlation between z_f and M_{cen} . These two opposing trends explain the suppression of the correlation strength with increased mass-mixing. Interestingly, the correlation strength for the other two input features appear to be largely impervious to mass-mixing.

Despite the disparity in which formation time maximizes the correlation strength, in what follows, we proceed with using z_{50} as our principal MAH summary statistic. This is motivated by the fact that $f = 0.5$ is a good compromise for which all three observables reveal a significant correlation strength and by the fact that z_{50} is widely used in the literature, thereby facilitating comparisons with other studies.

4.2. Random Forest Regression

Random Forest Regression (RFR) is a supervised machine learning method designed to capture complex, non-linear relationships between a series of input features quantified by the vector \mathbf{x} and a single continuous target variable (Breiman et al. 1984). The algorithm operates by constructing an ensemble of decision trees, each of which recursively partitions the input feature space into nodes that are increasingly homogeneous in terms of the target variable. In the context of regression, the impurity of a node is measured using the mean squared error

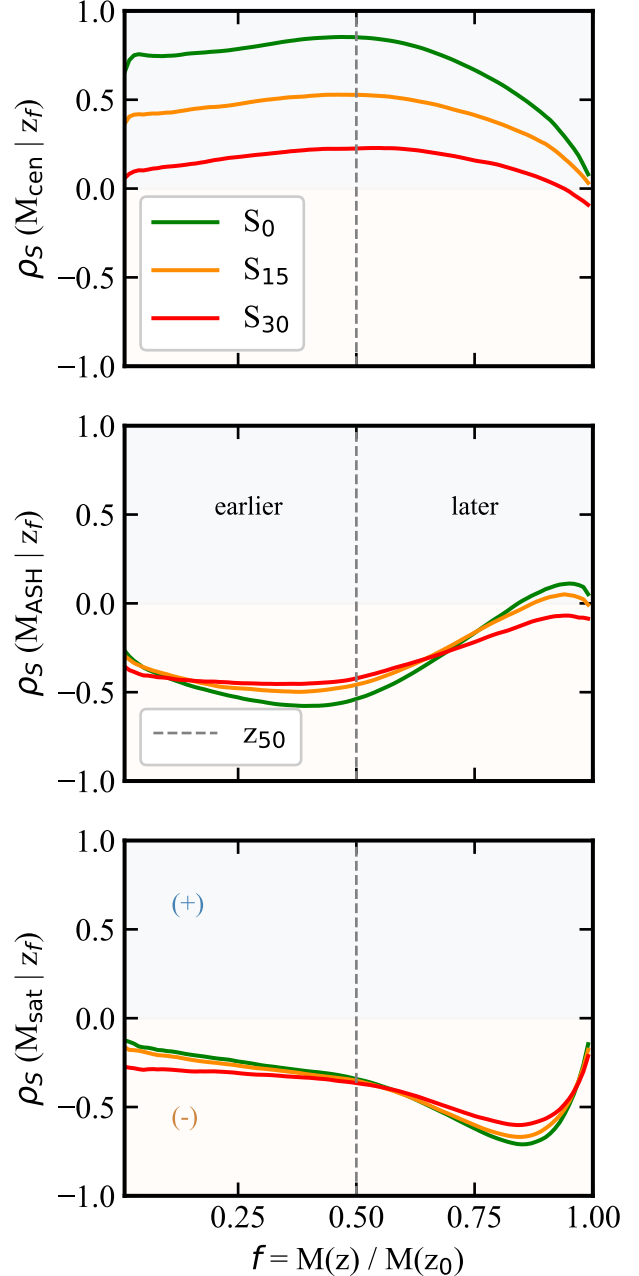


Figure 10. The correlations between each observable stellar mass component and halo formation times. Here we compute z_f on a discrete grid of mass fractions $f = M(z)/M(z_0)$ (where z_{37} would correspond to the redshift at which a halo had formed 37% of its present-day mass). The colored lines show the rank-order correlation coefficient as measured across the 10,000 galaxies in each of the three merger tree samples (S_0 , S_{15} and S_{30}). The vertical dashed line indicates z_{50} and the shaded colored regions distinguish between positive and negative correlations. **Top Panel:** the correlations between z_f and M_{cen} , **Middle Panel:** the correlations between z_f and M_{ASH} and finally, **Bottom Panel:** the correlations between z_f and M_{sat} .

(MSE):

$$\text{MSE} = \frac{1}{n} \sum_{i=1}^n (y_i - \bar{y})^2 \quad (18)$$

where n is the number of training objects that pass the node, y_i are the observed target values, and \bar{y} is their mean. Each split is chosen to minimize the sum of impurities, weighted by n ,

the number of objects in each node, producing regions where the target values are as similar as possible. Each terminal node in a tree assigns a value for the target variable based on the training data that fall into that region, which forms the basic predictive unit used in random forest regression.

Single decision trees are prone to overfitting the training data and typically exhibit large variance in their predictions (Breiman 2001). RFRA overcome this limitation by averaging over a large collection of decision trees, each trained on a bootstrap sample of the input data. This procedure, known as “bootstrap aggregation”, makes the ensemble less sensitive to noise in the training set. Another important aspect is “feature randomness”: at each node, the split is selected from a random subset of input features. This decorrelates the trees and further reduces the variance of their predictions.

The final RFRA prediction of a target variable for a new (as in, not part of the training data) input feature set \mathbf{x} is then obtained by averaging over the predictions of all T trees in the ensemble:

$$f(\mathbf{x}) = \frac{1}{T} \sum_{t=1}^T f_t(\mathbf{x}), \quad (19)$$

where $f_t(\mathbf{x})$ is the prediction of the t -th tree.

RFRA also naturally quantify “feature importance” by measuring the total reduction in impurity attributable to splits on a specific input feature, summed over all nodes and averaged across the ensemble of trees. In other words, input features that consistently produce large reductions in impurity carry more information about the target variable than those that do not. This interpretability is a primary motivation for our choice of RFRA over other machine-learning methods.

Model performance is evaluated using the coefficient of determination, R^2 , which measures the fraction of variance in the target variable explained by the ensemble prediction. For a set of test objects with observed target values y_i and RFRA predictions $\hat{y}_i = f(\mathbf{x}_i)$, R^2 is defined as

$$R^2 = 1 - \frac{\sum_i (y_i - \hat{y}_i)^2}{\sum_i (y_i - \bar{y})^2}, \quad (20)$$

where \bar{y} is the mean of the observed target values in the test sample. The coefficient of determination ranges from 0 to 1, with $R^2 = 1$ representing perfect predictive accuracy.

Attempting to capture the complex mapping between input features and target variables (see Section 4.1) using simple parametric models would be inefficient and overly contrived. Our assessment of the algorithm’s performance therefore relies on relative feature importance, R^2 scores, and visual inspection of “True vs. Predicted” scatter plots. In this analysis, we make use of the `scikit-learn` Python package (Pedregosa et al. 2011). In practice, RFRA have only a few hyperparameters that require tuning, such as the number of trees in the forest and the maximum depth of each tree. Because the final results are relatively insensitive to the exact choices of these hyperparameters, we empirically tuned them by selecting the combination that yielded the best R^2 scores without substantially increasing computational cost.

4.3. Training the Algorithms

Throughout the analysis, we use an 80% / 20% split for the training and validation sets, respectively. Each inference test is performed using data from one of our three merger tree samples (S_0, S_{15}, S_{30}). Recall that each merger tree sample has

10,000 unique galaxy realizations. Therefore, we train each algorithm on 8,000 trees selected at random during initialization and measure R^2 with respect to the remaining 2,000 trees. In this way, the algorithms are never evaluated on data that were used for training.

As mentioned previously, the algorithms are designed to learn the mapping between a set of input features and a single target variable. This means that for every merger tree sample, we train three RFRA, one for each of the target variables. We adopt the following shorthand: an RFRA trained on the S_{15} sample to recover the N_{90} target variable is denoted $f_{15}^{N_{90}}$. Similarly, an RFRA trained on the S_0 sample to recover the z_{50} target variable would be denoted $f_0^{z_{50}}$, etc. Using only the fiducial input features [M_{cen} , M_{ASH} and M_{sat}], we train a total of $3 \times 3 = 9$ algorithms. We show the results of our RFRA-based inference tests in Figures 11, 12, 13 for the z_{50} , N_{90} , and $M_{\text{acc}}^{\text{MMP}}$ target variables, respectively. The top rows of these figures show the relative feature importance, and the bottom rows show the True vs. Predicted scatter plots.

4.4. The z_{50} Target Variable

The inference tests on the z_{50} target variable differ significantly across the three merger tree samples. This is evident from the top three panels of Figure 11 that show the relative feature importance of each test. Starting with the $f_0^{z_{50}}$ algorithm, it finds almost no relevant information in the M_{ASH} and M_{sat} input features, but performs well with an $R^2 = 0.76$. This is a direct consequence of how we model $M_{\text{in-situ}}$, which results in more massive centrals in halos that assemble earlier (see Section 2.5) and the fact that the S_0 sample is free of host halo mass-mixing. In other words, the $f_0^{z_{50}}$ algorithm illustrates “a best case scenario” where the halo mass of the host galaxy is known perfectly.

The $f_{15}^{z_{50}}$ and $f_{30}^{z_{50}}$ algorithms rely less on the direct link between M_{cen} and z_{50} and more on the information content of the other two features. Unfortunately, the host-halo mass-mixing causes a downgrade in R^2 scores compared to the $f_0^{z_{50}}$ algorithm. This makes sense given that a significant fraction of the variance in the target variable comes from variance in host halo masses, rather than from variance in the input features. Interestingly, comparing the $f_{15}^{z_{50}}$ and $f_{30}^{z_{50}}$ algorithms, the additional 0.15 dex scatter in host halo masses in the S_{30} sample does not significantly impact the inference of z_{50} . This is likely due to the fact that their underlying z_{50} distributions are very similar (see Figures 2 & 16).

4.5. The N_{90} Target Variable

Figure 12 shows the results for the N_{90} target variable. The $f_0^{N_{90}}$ algorithm is entirely informed by the M_{ASH} input feature, but performs remarkably well with $R^2 = 0.91$. This highlights the strong anti-correlation discussed in Section 4.1, showing that halos with more massive ASHs are formed by fewer significant progenitors.

As discussed in Section 4.1, this anti-correlation is a consequence of the relatively steep slope of the SHMR at the low mass end, which implies that more massive subhalos contribute a stellar mass that is disproportionately high. Obviously, the success of the $f_0^{N_{90}}$ algorithm is also aided by the fact that host halo mass-mixing is neglected.

In the case of the $f_{15}^{N_{90}}$ and $f_{30}^{N_{90}}$ algorithms, the inclusion of host halo mass-mixing makes the algorithms less reliant on M_{ASH} . As with the z_{50} target variable, this reduces the

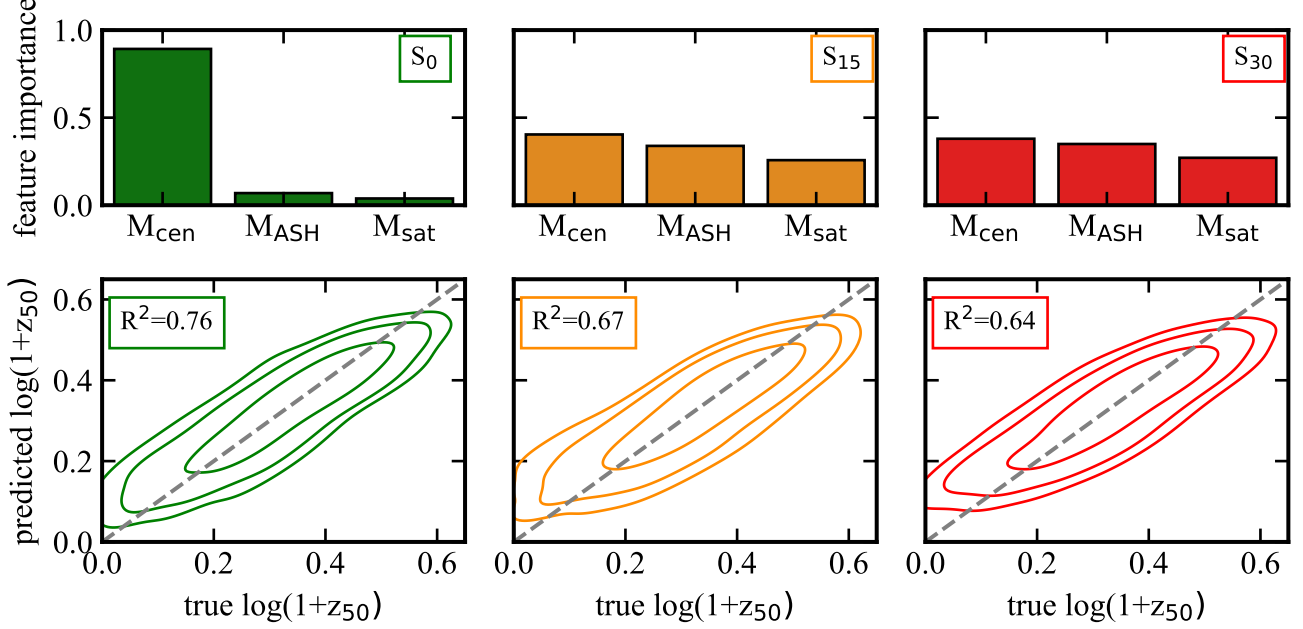


Figure 11. The results of the RFRA for the z_{50} target variable. **Top three panels:** The relative importance of the three input features [M_{cen} , M_{ASH} and M_{sat}] for all three merger tree samples. **Bottom three panels:** The True vs. Predicted contours for the 2000 galaxies used in the validation step. The contours show the 1, 2, and 3σ confidence intervals from a kernel density estimator. Legends show the algorithm's R^2 score which can be interpreted as proportion of variance in z_{50} that can be explained by the independent features in the model. Notice that the S_0 inference test is almost entirely reliant on the M_{cen} input feature but, when host halo mass-mixing is included, M_{ASH} and M_{sat} become more relevant. Furthermore, because the R^2 score worsens from S_0 to S_{30} , its clear that M_{DM} should be constrained before inferring z_{50} .

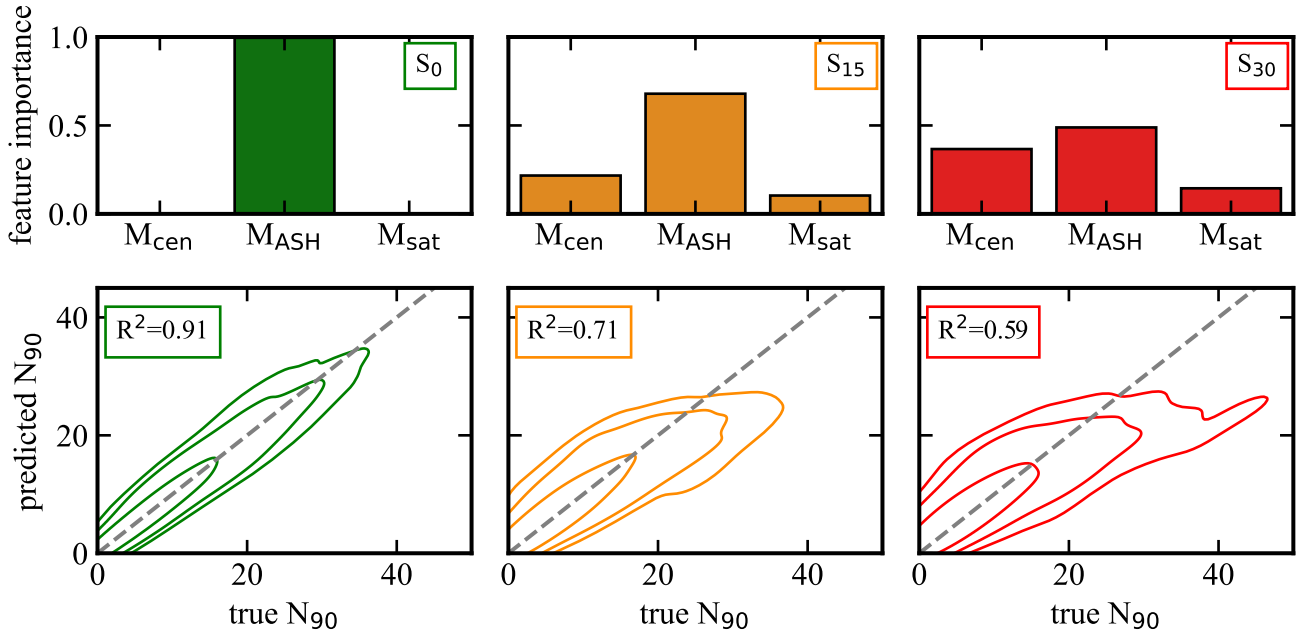


Figure 12. The same as Figure 11 but for the N_{90} target variable. Notice that the S_0 inference test is entirely reliant on the M_{ASH} input feature but, when host halo mass-mixing is included, M_{cen} and M_{sat} become more relevant. Once again, because the R^2 score worsens from S_0 to S_{30} , its important to get a handle on the underlying host halo masses before trying to infer N_{90} .

R^2 performance relative to the $f_0^{N_{90}}$ algorithm. Clearly, by increasing host halo mass-mixing, the inference of N_{90} from the input features becomes less reliable. In fact, both the $f_{15}^{N_{90}}$ and $f_{30}^{N_{90}}$ algorithms have a tendency to overpredict N_{90} for galaxies with the largest number of significant progenitors.

4.6. The $M_{\text{acc}}^{\text{MMP}}$ Target Variable

Unlike z_{50} and N_{90} , the inference tests on the $M_{\text{acc}}^{\text{MMP}}$ target do not vary significantly across the three merger tree samples. Figure 13 shows that both the M_{ASH} and M_{sat} features are important for all three samples. This can be understood as follows. If $M_{\text{acc}}^{\text{MMP}}$ is large, and remains largely intact, it makes a large contribution to M_{sat} . On the other hand, if it does not survive, it makes a large contribution to M_{ASH} .

Interestingly, $M_{\text{acc}}^{\text{MMP}}$ is the only target variable whose prediction accuracy increases with the inclusion of host halo mass-mixing. This owes to the fact that $M_{\text{acc}}^{\text{MMP}}$, M_{ASH} , and M_{sat} are all strongly correlated with host halo mass (more massive hosts have more massive progenitors, more massive stellar halos and a more massive satellite population). Consequently, the range of $M_{\text{acc}}^{\text{MMP}}$ values increases with increased mass-mixing, as is clearly evident in the lower panels of Figure 13. Given that realistic samples will always include a non-negligible amount of mass-mixing, we can therefore conclude that observations of M_{ASH} and M_{sat} can give a surprisingly good handle on $M_{\text{acc}}^{\text{MMP}}$.

5. DISCUSSION

5.1. Galaxy Assembly Bias

An important outstanding question in galaxy formation theory is whether there is evidence for galaxy assembly bias; the correlation between galaxy properties and halo formation time at fixed halo mass (see e.g., [Mo et al. 2010](#); [Zentner et al. 2014](#); [Hearin et al. 2015](#); [Zu & Mandelbaum 2018](#); [Wechsler & Tinker 2018](#); [Wang et al. 2022](#)). The main problem lies in that it is difficult to obtain reliable estimates for the formation times of individual halos. As shown in Section 4, our model predicts that M_{cen} , M_{ASH} , and M_{sat} are all correlated with halo formation time, albeit only weakly (see also Figure 16 in Appendix B). This suggests that observations of M_{cen} , M_{ASH} and M_{sat} , can in principle be used to constrain z_{50} . Indeed, we have demonstrated the ability to infer an estimate of $\log[1 + z_{50}]$ with an error that is roughly 50 to 60 percent of its variance (as estimated from $\sqrt{1 - R^2}$). Although far from perfect, this should be sufficient to split any sample of galaxies in early- and late-forming systems and test for galaxy assembly bias.

However, this comes with an important caveat: tests of assembly bias must control for halo mass and are therefore ideally performed using halos of identical mass. Unfortunately, selecting galaxies directly by halo mass is extremely difficult. Typically, samples are constructed by imposing cuts on stellar mass, luminosity, or surface brightness in an attempt to select a narrow range of host halo mass ([Carlsten et al. 2022](#); [Mao et al. 2024](#); [Guzmán 2024](#)). Given the non-zero scatter in the SHMR, realistic data samples will unavoidably be subject to significant host halo mass-mixing. Given the shape and scatter of the SHMR, the extent of this mass-mixing is expected to be larger for brighter galaxies (see e.g., [More et al. 2009](#)). Unfortunately, as shown in Figure 11, host halo mass-mixing significantly weakens the precision of the inferred halo formation time. Hence, unless halo mass estimates can be made on individual galaxies, for example from gravitational lensing or satellite kinematics, the unknown distribution of M_{DM}

will significantly weaken the inference of assembly time from observational measurements of M_{cen} , M_{ASH} and M_{sat} .

To illustrate the extent of this challenge, Figure 14 plots the host halo masses vs. formation times of galaxies in the S_{30} sample, color coded based on M_{cen} (left panel), M_{ASH} (middle panel) and M_{sat} (right panel). In all three cases, the color gradient is much more pronounced in the M_{DM} -direction than in the direction of $\log(1 + z_{50})$, indicating that all three ‘observables’ depend more strongly on halo mass than on halo formation time. This highlights the challenges one faces when trying to infer properties such as formation time from a sample of galaxies for which the host halo masses are unknown or uncertain. Nevertheless, our tests based on samples S_{15} and S_{30} suggest that reliable measurement of M_{cen} , M_{ASH} , and M_{sat} still contains valuable information useful for inferring MAHs. In forthcoming work, we extent this analysis by examining whether such observables can be used to simultaneously infer both halo mass and halo formation time.

5.2. Caveats

The model that we have used here to study the stellar halos of Milky Way-like galaxies is subject to a number of caveats:

5.2.1. In-Situ Stellar Halos

Stellar halos are expected to contain a mixture of ex-situ and in-situ populations, with the relative contribution depending on galactocentric radius, the star formation history of the central galaxy, and the assembly history of the host halo ([Bullock & Johnston 2005](#); [Cooper et al. 2010](#); [Deason et al. 2016](#)). However, throughout this work, we only model the *ex-situ* component. As a result, our predictions are best interpreted as lower limits on the total stellar halo mass of MW-like galaxies.

In-situ halo stars are generally confined to the inner halo ([Cooper et al. 2013](#); [Font et al. 2020](#)), where they arise from processes such as disk heating ([Tissera et al. 2013](#)) and bulge-driven evolution, including feedback and secular mechanisms ([Zolotov et al. 2009](#)). Beyond galactocentric radii of $\sim 20 - 30$ kpc, the stellar halos of MW-like galaxies are expected to be dominated by accreted (ex-situ) stars ([Cooper et al. 2015](#); [Font et al. 2020](#); [Wright et al. 2024](#)). Simulation-based studies find that the in-situ contribution to the stellar halo mass of MW-like systems is typically subdominant, though with substantial scatter across different suites. Reported in-situ fractions span a wide range from $\sim 5\%$ to 40% , depending on numerical resolution and subgrid prescriptions ([Rodriguez-Gomez et al. 2016](#); [Davison et al. 2020](#); [Santistevan et al. 2020](#); [Cooper et al. 2025](#); [Celiz et al. 2025](#)). It is unclear whether this diversity is due to physical halo-to-halo variance or to uncertain baryonic physics and/or ambiguity in defining the stellar halo.

From an observational perspective, extragalactic measurements of stellar halos rely heavily on projected radial cuts (e.g., [Merritt et al. 2016](#)), which tend to mix in-situ and ex-situ populations ([Sanderson et al. 2018](#)). This makes it unfeasible to isolate and quantify the in-situ contribution in a model-independent manner ([Rodriguez-Gomez et al. 2016](#)). Nevertheless, recent observational studies of individual systems are broadly consistent with the picture that ex-situ stars dominate the density profiles and substructure signatures of MW-like stellar halos, particularly at large radii ([Bell et al. 2008](#); [Williams et al. 2025](#)).

By restricting our analysis to the ex-situ component, we focus on the stellar material that directly traces satellite accretion and hierarchical assembly. This modeling choice enables ro-

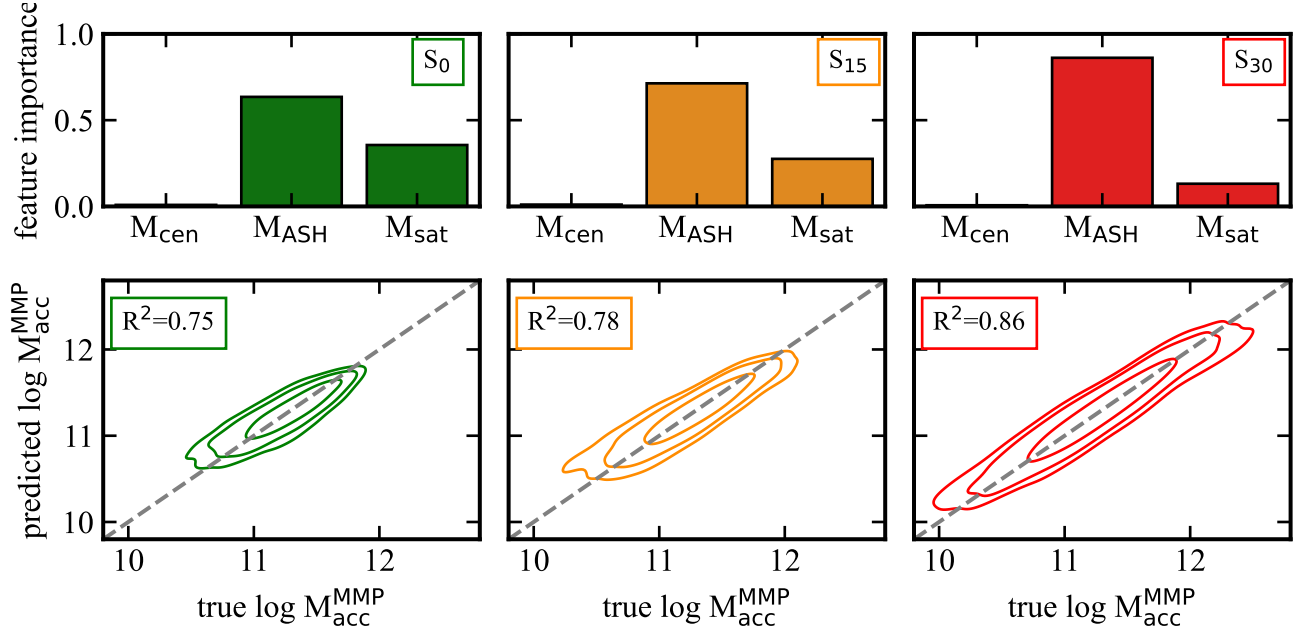


Figure 13. The same as Figure 11 but for the $M_{\text{acc}}^{\text{MMP}}$ target variable. Here the M_{cen} feature holds almost effectively no information relevant to $M_{\text{acc}}^{\text{MMP}}$ and M_{ASH} is dominant across all three samples. Unlike the other two target variables, the R^2 scores actually increase from S_0 to S_{30} which means that host halo mass-mixing does not muddle inference on the $M_{\text{acc}}^{\text{MMP}}$ target variable.

bust comparisons with simulation-based studies that can trivially measure ex-situ fractions by selecting star particles that were not formed inside the main progenitor. Finally, because our M_{ASH} component does not constitute the entire stellar halo mass budget, direct comparisons with observational measurements should be interpreted with appropriate caution.

5.2.2. Satellite Quenching

By assigning satellite galaxies stellar masses based on the SHMR at the redshift of accretion, we have effectively assumed that galaxies quench their star formation upon accretion. Although it is well known that satellite galaxies experience enhanced quenching compared to centrals (e.g., Weinmann et al. 2006; van den Bosch et al. 2008), the assumption of instantaneous quenching upon accretion is clearly oversimplified. Indeed, a significant fraction of satellite galaxies are star forming (Weinmann et al. 2006; Geha et al. 2024) and several studies have shown that there is a typical delay time of the order of 1-2 Gyr between satellite accretion and quenching (Wetzel et al. 2013; Maier et al. 2019; Akins et al. 2021; Pathak et al. 2025). These delays are believed to roughly reflect the time it takes a satellite to reach its first peri-centric passage, where ram-pressure-stripping is most effective at removing gas and quenching the system (Gunn & Gott 1972; Tollet et al. 2017). However, as long as satellite galaxies do not significantly increase their stellar mass due to ongoing star formation after accretion—as found by several recent studies (e.g., Munshi et al. 2021; Engler et al. 2021; Shipp et al. 2024; Rodríguez-Cardoso et al. 2025)—this oversimplification should not have a large effect on the results presented here.

5.2.3. Dark Matter Density Profiles

Throughout, we have assumed that all dark matter halos have cuspy NFW density profiles. In reality, baryonic processes can significantly modify the (central) density profiles of halos (Blumenthal et al. 1986; Pontzen & Governato 2012; Zolotov

et al. 2012), which in turn can have a significant impact on their tidal evolution (Peñarrubia et al. 2010; Errani & Peñarrubia 2020). Similarly, if dark matter is self-interacting rather than collisionless, the halos may be cored or have undergone core-collapse (Spergel & Steinhardt 2000; Balberg et al. 2002), both of which will significantly impact their tidal evolution. We leave it for future work to examine how modifications of the subhalo/satellite density profiles impact the statistics of M_{ASH} and M_{sat} .

6. CONCLUSIONS

We have presented a new model based on SatGen for the construction of stellar halos from the disrupted remains of accreted satellite galaxies. Unlike computationally expensive hydrodynamical simulations that are hampered by limited sample sizes and numerical artifacts, our semi-analytic approach efficiently samples the full diversity of merger histories essential for probing the various stochastic processes at play during galaxy formation. Using three different merger tree samples with a total of 30,000 unique mass accretion histories of MW-like host halos, we have investigated correlations between several observables and characteristics of the host halo’s assembly history.

Specifically, we have focused on three main present-day observables: M_{cen} , the stellar mass of the main host galaxy, M_{ASH} the accreted stellar halo mass, and M_{sat} the cumulative stellar mass in surviving satellites. We studied how these quantities are impacted by various sources of stochasticity in the assembly of MW-like galaxies, and how they are correlated with characteristics of the host halo’s MAH. Our main results are as follows:

- On average, $\sim 95\%$ of the present-day ASH comes from satellite systems that have been completely disrupted by tidal forces or merged directly with the central. The remaining $\sim 5\%$ originates from surviving satellite systems that are in the process of being tidally stripped.

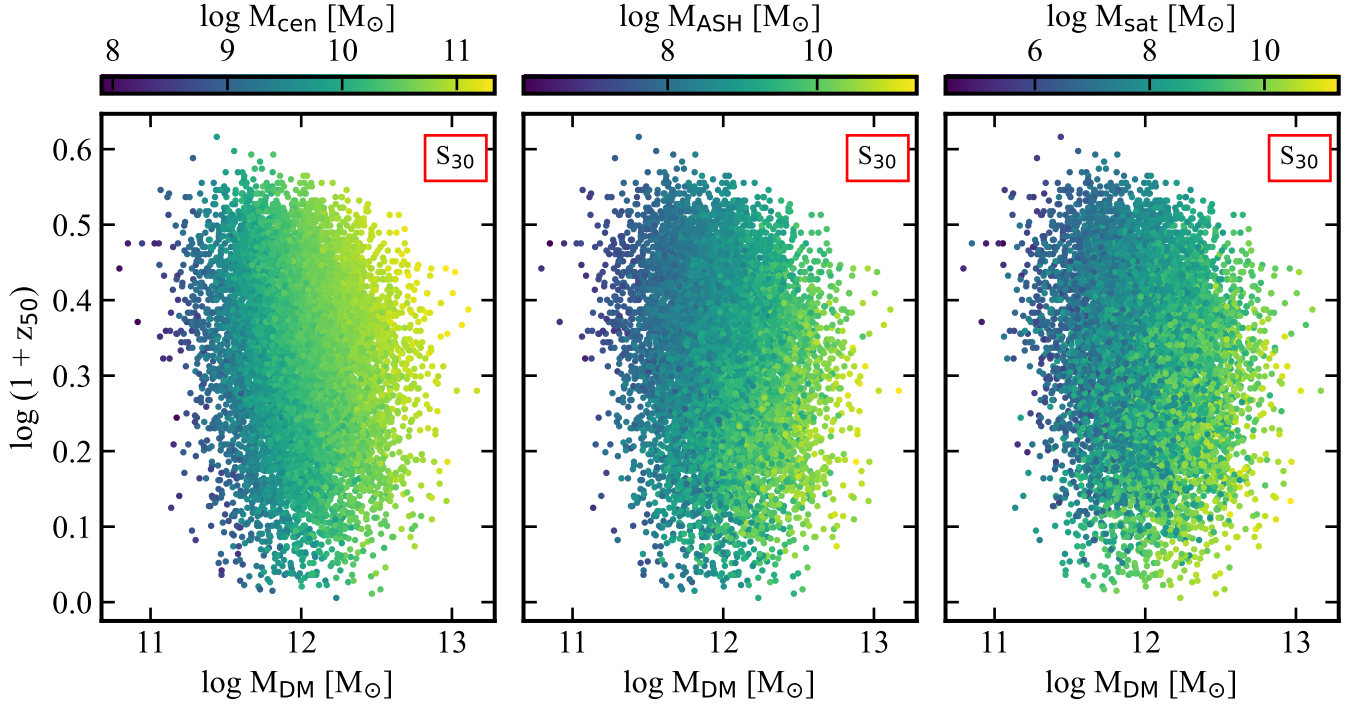


Figure 14. Scatter plots of M_{DM} and z_{50} in the S_{30} merger tree sample. **Left Panel:** Here the distribution is colored by the M_{cen} input feature and shows a clear color gradient in the x-direction indicative of the assumed SHMR. **Middle Panel:** Here the distribution is colored by the M_{ASH} input feature and shows a clear color gradient in the x-direction alongside a noisy color gradient in the y-direction indicative of the fact that later forming host halos have more massive accreted stellar halos. **Right Panel:** Here the distribution is colored by the M_{sat} input feature and qualitatively demonstrates the same behavior as the M_{ASH} component.

- Because of dynamical friction, more massive satellites are less likely to survive to the present. Specifically for the S_0 sample, we measure the accretion redshift above which the survival probability is less than 50% decreases from $z_{\text{acc}} = 2.89$ for satellites with $m_* \sim 10^5 M_{\odot}$, to $z_{\text{acc}} = 0.70$ for $m_* \sim 10^7$, to $z_{\text{acc}} = 0.32$ for $m_* \sim 10^9 M_{\odot}$.
- Among the surviving systems, more massive satellites have been accreted more recently. The most massive surviving satellite in the S_0 sample was accreted between $z = 0.11$ and $z = 0.89$ (16-84 percentile range). Furthermore, we measure the probability that *any* first-order surviving satellite (with a stellar mass at accretion $m_* > 10^5$) was accreted prior to $z = 1.0$ ($z = 3.0$) is 0.45 (0.06).
- Despite the prevalence of satellites being cannibalized by the central galaxy, the ex-situ fraction of the final stellar mass of the central galaxy is negligible ($\lesssim 1\%$) even when our free parameters are set to maximize the contribution (see Appendix A). This is in agreement with several previous studies (e.g., Yang et al. 2013; Lu et al. 2015), that find the vast majority stars in the central galaxy of MW-like hosts formed in-situ.
- Given the steep slope of the low-mass end of the SHMR assumed, the most massive progenitor satellite typically plays a decisive role in setting M_{ASH} (Cooper et al. 2013; Amorisco 2017; Elias et al. 2018; Rey & Starkenburg 2022). This is particularly true for late-forming galaxies (i.e., those with a small z_{50}) where the survival or destruction/merger of the most massive progenitor leads to order-of-magnitude differences in the accreted stellar halo mass (see Figure 6).
- The majority of the present-day ASH originates from a small

number of progenitors. The median number of mass-ranked progenitors that, when combined, contribute 90% to the accreted stellar halo, is 6 with a broad 16-84 percentile range of 1 to 11 (see Figure 7). This indicates that accreted stellar halos of MW-like galaxies are subject to large halo-to-halo variance sourced by the stochasticity of the accretion masses, accretion redshifts, and orbits of a handful of the most massive accretion events (see also Deason et al. 2016; Monachesi et al. 2019).

- At fixed halo mass, the main sources of variance in M_{ASH} and M_{sat} are stochasticity in mass accretion histories and initial orbital satellite properties. Scatter in the SHMR of accreted satellites makes a negligible contribution and will therefore be difficult to constrain given observations of stellar halos and/or the surviving satellite populations (see also Monzon et al. 2024).
- Correlating our three observables with the redshift z_f at which the main progenitor has assembled a fraction f of its final mass, for different values of f , we find that different stellar components trace different formation epochs of dark matter assembly (see Figure 10). For M_{cen} and M_{ASH} the correlations are maximized for $f \sim 0.5$, indicating that they carry information regarding the early formation history of the host halo. On the other hand, M_{sat} is more indicative of the host halo’s more recent assembly, with a maximum (anti)correlation for $f \sim 0.85$.
- In realistic samples of stellar halos, host halo mass-mixing is unavoidable and is likely to be the dominant source of scatter in M_{ASH} and M_{sat} (see Figure 8). We find that adding 0.15 (0.3) dex of scatter in host halo mass boosts the scatter in M_{ASH} from ~ 0.4 dex to ~ 0.5 (0.7) dex. In general,

host halo mass-mixing significantly weakens correlations between observable input features and target variables. In particular, host halo mass-mixing leads to a degradation in the recovery of z_{50} and N_{90} (see Figures 11 and 12). In contrast, because $M_{\text{acc}}^{\text{MMP}}$ traces M_{DM} , recovery performance actually improves when host halo masses are mixed (see Figure 13).

- Using random forest regression, we have demonstrated that the combination of M_{cen} , M_{ASH} , and M_{sat} observables can be used to infer properties of the host halo’s assembly history despite the large variance due to stochasticity in the orbital properties of satellite galaxies.

In future work, we will use the model developed here to examine stellar halos and satellite populations across a much wider range in host halo mass and investigate how their properties may inform characteristics of the SHMR, especially at the low-mass end.

7. ACKNOWLEDGMENTS

The authors thank Yao-Yuan Mao, Marla Geha, Yasmeen Asali, Peter Behroozi, Ethan Nadler, and Raphael Errani for valuable discussions. FvDB is supported by the National Science Foundation (NSF) through grant AST-2307280. This work was performed in part at the Kavli Institute for Theoretical Physics (KITP) in Santa Barbara, which is supported in part by the National Science Foundation under Grant No. NSF PHY-174895.

REFERENCES

Abadi M. G., Navarro J. F., Steinmetz M., Eke V. R., 2003, *ApJ*, **591**, 499

Abraham R. G., van Dokkum P. G., 2014, *PASP*, **126**, 55

Aihara H., the HSC Collaboration 2018, *Publications of the Astronomical Society of Japan*, **70**, S4

Akins H. B., Christensen C. R., Brooks A. M., Munshi F., Applebaum E., Engelhardt A., Chamberland L., 2021, *ApJ*, **909**, 139

Allen M., Behroozi P., Ma C.-P., 2019, *MNRAS*, **488**, 4916

Amorisco N. C., 2017, *MNRAS*, **469**, L48

Asali Y., et al., 2025, *arXiv e-prints*, p. arXiv:2509.25335

Balberg S., Shapiro S. L., Inagaki S., 2002, *ApJ*, **568**, 475

Behroozi P., Wechsler R. H., Hearin A. P., Conroy C., 2019, *MNRAS*, **488**, 3143

Bell E. F., et al., 2008, *ApJ*, **680**, 295

Belokurov V., Erkal D., Evans N. W., Koposov S. E., Deason A. J., 2018, *MNRAS*, **478**, 611

Binney J., Tremaine S., 2008, *Galactic Dynamics*: Second Edition. Princeton University Press

Blumenthal G. R., Faber S. M., Flores R., Primack J. R., 1986, *ApJ*, **301**, 27

Bonaca A., Price-Whelan A. M., 2025, *New A Rev*, **100**, 101713

Breiman L., 2001, *Machine Learning*, **45**, 5

Breiman L., Friedman J., Olshen R. A., Stone C. J., 1984, *Classification and Regression Trees*, 1st edn. Chapman and Hall/CRC, doi:10.1201/9781315139470

Bullock J. S., Johnston K. V., 2005, *ApJ*, **635**, 931

Bullock J. S., Kolatt T. S., Sigad Y., Somerville R. S., Kravtsov A. V., Klypin A. A., Primack J. R., Dekel A., 2001, *MNRAS*, **321**, 559

Carlsten S. G., Greene J. E., Beaton R. L., Danieli S., Greco J. P., 2022, *ApJ*, **933**, 47

Celiz B. M., Navarro J. F., Abadi M. G., 2025, *arXiv e-prints*, p. arXiv:2510.18971

Chabrier G., 2003, *PASP*, **115**, 763

Chandrasekhar S., 1943, *ApJ*, **97**, 255

Chiang B. T., van den Bosch F. C., Schive H.-Y., 2024, *arXiv e-prints*, p. arXiv:2411.03192

Christensen C. R., Brooks A. M., Munshi F., Riggs C., Van Nest J., Akins H., Quinn T. R., Chamberland L., 2024, *ApJ*, **961**, 236

Conroy C., Gunn J. E., 2010, *ApJ*, **712**, 833

Cooper A. P., et al., 2010, *MNRAS*, **406**, 744

Cooper A. P., D’Souza R., Kauffmann G., Wang J., Boylan-Kolchin M., Guo Q., Frenk C. S., White S. D. M., 2013, *MNRAS*, **434**, 3348

Cooper A. P., Parry O. H., Lowing B., Cole S., Frenk C., 2015, *MNRAS*, **454**, 3185

Cooper A. P., Frenk C. S., Hellwing W. A., Bose S., 2025, *arXiv e-prints*, p. arXiv:2501.13317

Danieli S., Greene J. E., Carlsten S., Jiang F., Beaton R., Goulding A. D., 2023, *ApJ*, **956**, 6

Davison T. A., Norris M. A., Pfeffer J. L., Davies J. J., Crain R. A., 2020, *MNRAS*, **497**, 81

Deason A. J., Belokurov V., 2024, *New A Rev*, **99**, 101706

Deason A. J., Belokurov V., Weisz D. R., 2015, *MNRAS*, **448**, L77

Deason A. J., Mao Y.-Y., Wechsler R. H., 2016, *ApJ*, **821**, 5

Deason A. J., Belokurov V., Sanders J. L., 2019, *MNRAS*, **490**, 3426

Diemand J., Kuhlen M., Madau P., 2007, *ApJ*, **667**, 859

Diemer B., Behroozi P., Mansfield P., 2024, *MNRAS*, **533**, 3811

Dropulic A., Shipp N., Kim S., Mezghanni Z., Necib L., Lisanti M., 2025, *ApJ*, **990**, 162

Elias L. M., Sales L. V., Creasey P., Cooper M. C., Bullock J. S., Rich R. M., Hernquist L., 2018, *MNRAS*, **479**, 4004

Engler C., et al., 2021, *MNRAS*, **500**, 3957

Errani R., Peñarrubia J., 2020, *MNRAS*, **491**, 4591

Errani R., Peñarrubia J., Walker M. G., 2018, *MNRAS*, **481**, 5073

Fattahi A., et al., 2019, *MNRAS*, **484**, 4471

Font A. S., et al., 2020, *MNRAS*, **498**, 1765

Forourhar Moreno V. J., Fattahi A., Deason A. J., Henstridge F., Benítez-Llambay A., 2025, *MNRAS*,

Geen S., Slyz A., Devriendt J., 2013, *MNRAS*, **429**, 633

Geha M., et al., 2017, *ApJ*, **847**, 4

Geha M., et al., 2024, *arXiv e-prints*, p. arXiv:2404.14499

Gilhuly C., et al., 2022, *ApJ*, **932**, 44

Green S. B., van den Bosch F. C., 2019, *MNRAS*, **490**, 2091

Green S. B., van den Bosch F. C., Jiang F., 2021, *MNRAS*, **503**, 4075

Grimozzi S. E., Font A. S., de Rossi M. E., 2024, *MNRAS*, **530**, 95

Gunn J. E., Gott J. Richard I., 1972, *ApJ*, **176**, 1

Guzmán R., 2024, in EAS2024, European Astronomical Society Annual Meeting, p. 1990

Harmse B., Monachesi A., Bell E. F., de Jong R. S., Bailin J., Radburn-Smith D. J., Holwerda B. W., 2017, *MNRAS*, **466**, 1491

Hearin A. P., Watson D. F., van den Bosch F. C., 2015, *MNRAS*, **452**, 1958

Helmi A., 2020, *ARA&A*, **58**, 205

Helmi A., Babusiaux C., Koppelman H. H., Massari D., Veljanoski J., Brown A. G. A., 2018, *Nature*, **563**, 85

Jiang F., van den Bosch F. C., 2014, *MNRAS*, **440**, 193

Jiang F., van den Bosch F. C., 2017, *MNRAS*, **472**, 657

Jiang F., Dekel A., Freundlich J., van den Bosch F. C., Green S. B., Hopkins P. F., Benson A., Du X., 2021, *MNRAS*, **502**, 621

Joshi G. D., Pontzen A., Agertz O., Rey M. P., Read J., Renaud F., 2024, *MNRAS*, **528**, 2346

Joshi G. D., Pontzen A., Agertz O., Read J., Rey M. P., 2025, *MNRAS*, **544**, 2811

Kado-Fong E., et al., 2025, *ApJ*, **994**, 231

Khoperskov S., et al., 2023, *A&A*, **677**, A90

King I., 1962, *AJ*, **67**, 471

Kong H., Boylan-Kolchin M., Bullock J. S., 2025, *arXiv e-prints*, p. arXiv:2503.10766

Koppelman H., Helmi A., Veljanoski J., 2018, *ApJL*, **860**, L11

Li Z.-Z., Zhao D.-H., Jing Y. P., Han J., Dong F.-Y., 2020, *ApJ*, **905**, 177

Lu Z., Mo H. J., Lu Y., Katz N., Weinberg M. D., van den Bosch F. C., Yang X., 2015, *MNRAS*, **450**, 1604

Maier C., Ziegler B. L., Haines C. P., Smith G. P., 2019, *A&A*, **621**, A131

Malhan K., et al., 2022, *ApJ*, **926**, 107

Mansfield P., Darragh-Ford E., Wang Y., Nadler E. O., Diemer B., Wechsler R. H., 2024, *ApJ*, **970**, 178

Mao Y.-Y., Geha M., Wechsler R. H., Weiner B., Tollerud E. J., Nadler E. O., Kalivayalil N., 2021, *ApJ*, **907**, 85

Mao Y.-Y., et al., 2024, *arXiv e-prints*, p. arXiv:2404.14498

Merritt A., van Dokkum P., Abraham R., Zhang J., 2016, *ApJ*, **830**, 62

Merritt A., Pillepich A., van Dokkum P., Nelson D., Hernquist L., Marinacci F., Vogelsberger M., 2020, *MNRAS*, **495**, 4570

Mo H., van den Bosch F. C., White S., 2010, *Galaxy Formation and Evolution*. Cambridge University Press

Monachesi A., et al., 2019, *MNRAS*, **485**, 2589

Monzon J. S., van den Bosch F. C., Mitra K., 2024, *ApJ*, **976**, 197

More S., van den Bosch F. C., Cacciato M., 2009, *MNRAS*, **392**, 917

Moster B. P., Somerville R. S., Maulbetsch C., van den Bosch F. C., Macciò A. V., Naab T., Oser L., 2010, *ApJ*, **710**, 903

Moster B. P., Naab T., White S. D. M., 2018, *MNRAS*, **477**, 1822

Munshi F., Brooks A. M., Applebaum E., Christensen C. R., Quinn T., Sliw S., 2021, *ApJ*, **923**, 35

Nadler E. O., et al., 2020, *ApJ*, **893**, 48

Naidu R. P., et al., 2021, *ApJ*, **923**, 92

Navarro J. F., Frenk C. S., White S. D. M., 1997, *ApJ*, **490**, 493

O’Leary J. A., Steinwandel U. P., Moster B. P., Martin N., Naab T., 2023, *MNRAS*, **520**, 897

Ogiya G., van den Bosch F. C., Hahn O., Green S. B., Miller T. B., Burkert A., 2019, *MNRAS*, **485**, 189

Orkney M. D. A., et al., 2022, *MNRAS*, **517**, L138

Parkinson H., Cole S., Helly J., 2008, *MNRAS*, **383**, 557

Pathak D., Christensen C. R., Brooks A. M., Munshi F., Wright A. C., Carter C., 2025, *ApJ*, **989**, 178

Penarrubia J., McConnachie A. W., Navarro J. F., 2008, *ApJ*, **672**, 904

Peñarrubia J., Benson A. J., Walker M. G., Gilmore G., McConnachie A. W., Mayer L., 2010, *MNRAS*, **406**, 1290

Pedregosa F., et al., 2011, *Journal of Machine Learning Research*, **12**, 2825

Planck Collaboration et al., 2020, *A&A*, **641**, A6

Pontzen A., Governato F., 2012, *MNRAS*, **421**, 3464

Proctor K. L., Ludlow A. D., Lagos C. d. P., Robotham A. S. G., 2024, *arXiv e-prints*, p. [arXiv:2407.11444](https://arxiv.org/abs/2407.11444)

Pu S.-Y., Cooper A. P., Grand R. J. J., Gómez F. A., Monachesi A., 2025, *ApJ*, **980**, 63

Rey M. P., Starkenburg T. K., 2022, *MNRAS*, **510**, 4208

Riley A. H., et al., 2024, *arXiv e-prints*, p. [arXiv:2410.09144](https://arxiv.org/abs/2410.09144)

Rodríguez-Cardoso R., et al., 2025, *A&A*, **698**, A303

Rodríguez-Gómez V., et al., 2016, *MNRAS*, **458**, 2371

Rodríguez-Puebla A., Primack J. R., Avila-Reese V., Faber S. M., 2017, *MNRAS*, **470**, 651

Sales L. V., Wetzel A., Fattahi A., 2022, *Nature Astronomy*, **6**, 897

Sanderson R. E., et al., 2018, *ApJ*, **869**, 12

Santistevan I. B., Wetzel A., El-Badry K., Bland-Hawthorn J., Boylan-Kolchin M., Bailin J., Faucher-Giguère C.-A., Benincasa S., 2020, *MNRAS*, **497**, 747

Santos-Santos I. M. E., Sales L. V., Fattahi A., Navarro J. F., 2022, *MNRAS*, **515**, 3685

Sawicki M., Arnouts S., Huang J., et al. 2019, *Monthly Notices of the Royal Astronomical Society*, **489**, 5202

Sharpe K., Naidu R. P., Conroy C., 2024, *ApJ*, **963**, 162

Shipp N., et al., 2024, *arXiv e-prints*, p. [arXiv:2410.09143](https://arxiv.org/abs/2410.09143)

Spergel D. N., Steinhardt P. J., 2000, *Phys. Rev. Lett.*, **84**, 3760

Taffoni G., Mayer L., Colpi M., Governato F., 2003, *MNRAS*, **341**, 434

Taylor J. E., Babul A., 2001, *ApJ*, **559**, 716

Tissera P. B., Scannapieco C., Beers T. C., Carollo D., 2013, *MNRAS*, **432**, 3391

Tollet É., Cattaneo A., Mamon G., Moutard T., van den Bosch F., 2017, preprint, ([arXiv:1707.06264](https://arxiv.org/abs/1707.06264))

Wang K., Mao Y.-Y., Zentner A. R., Guo H., Lange J. U., van den Bosch F. C., Mezini L., 2022, *arXiv e-prints*, p. [arXiv:2204.05332](https://arxiv.org/abs/2204.05332)

Wechsler R. H., Tinker J. L., 2018, *ARA&A*, **56**, 435

Weinmann S. M., van den Bosch F. C., Yang X., Mo H. J., 2006, *MNRAS*, **366**, 2

Wetzel A. R., Tinker J. L., Conroy C., van den Bosch F. C., 2013, *MNRAS*, **432**, 336

Williams D. J., et al., 2025, *ApJ*, **989**, 107

Wright A. C., et al., 2024, *ApJ*, **970**, 70

Yang X., Mo H. J., van den Bosch F. C., Zhang Y., Han J., 2012, *ApJ*, **752**, 41

Yang X., Mo H. J., van den Bosch F. C., Bonaca A., Li S., Lu Y., Lu Y., Lu Z., 2013, *ApJ*, **770**, 115

Zentner A. R., Bullock J. S., 2003, *ApJ*, **598**, 49

Zentner A. R., Hearin A. P., van den Bosch F. C., 2014, *MNRAS*, **443**, 3044

Zhao D. H., Jing Y. P., Mo H. J., Börner G., 2009, *ApJ*, **707**, 354

Zhu L., et al., 2022, *A&A*, **660**, A20

Zolotov A., Willman B., Brooks A. M., Governato F., Brook C. B., Hogg D. W., Quinn T., Stinson G., 2009, *ApJ*, **702**, 1058

Zolotov A., et al., 2012, *ApJ*, **761**, 71

Zu Y., Mandelbaum R., 2018, *MNRAS*, **476**, 1637

van den Bosch F. C., 2002, *MNRAS*, **331**, 98

van den Bosch F. C., Jiang F., 2016, *MNRAS*, **458**, 2870

van den Bosch F. C., Ogiya G., 2018, *MNRAS*, **475**, 4066

van den Bosch F. C., Aquino D., Yang X., Mo H. J., Pasquali A., McIntosh D. H., Weinmann S. M., Kang X., 2008, *MNRAS*, **387**, 79

van den Bosch F. C., Jiang F., Hearin A., Campbell D., Watson D., Padmanabhan N., 2014, *MNRAS*, **445**, 1713

van den Bosch F. C., Ogiya G., Hahn O., Burkert A., 2018, *MNRAS*, **474**, 3043

APPENDIX

A. IMPACT OF FREE PARAMETERS

In this appendix, we discuss how the three free parameters [β_{DF} , X_{merge} , and f_{cann}] in our model impact our results using four illustrative merger trees from the S_0 sample introduced in Section 3.4. Specifically, for each tree we consider $\beta_{\text{DF}} = [0.5, 1, 2]$, $X_{\text{merge}} = [-0.5, -1, -2]$, and $f_{\text{cann}} = [0.2, 0.5, 0.8]$. Note that for each parameter combination, the subhalos are initialized with satellite galaxies of the same size and stellar mass, and evolved along the same orbit. Hence, the differences in the final mass components arise solely from changes in the free parameters. The 27 unique parameter combinations are shown in Figure 15 for the *early* (crimson lines), *middle* (purple lines), *late* (teal lines), and *latest* (blue lines) merger trees.

The top row of panels in Figure 15 shows the M_{ASH} mass component as a function of the assumed strength of dynamical friction, β_{DF} (see Section 2.8). Similarly, the bottom row of panels in Figure 15 shows the M_{sat} mass component. We purposefully exclude the M_{cen} mass component from these figures because it is insensitive to our three free parameters, even when they are tuned to maximize the role of mergers in the assembly of the central galaxy. The three columns of panels distinguish between different assumed merging criteria (X_{merge}), as indicated. Finally, the different line styles distinguish between the assumed cannibalization fractions (f_{cann}). In the background of all panels, we show the 16-84 and 5-95

percentile extents of the corresponding mass components in the S_0 distributions.

Notice that although the absolute values of the different mass components depend strongly on the particular merger tree used, the *relative* changes in M_{ASH} and M_{sat} in response to $[\beta_{\text{DF}}$, X_{merge} , and f_{cann}] are minor. Figure 15 therefore emphasizes that the inherent sources of stochasticity in the M_{ASH} and M_{sat} components are far more dominant than systematic changes caused by our choice of free parameters. Recall that, using our fiducial model [$\beta_{\text{DF}} = 1$, $X_{\text{merge}} = -2.0$, and $f_{\text{cann}} = 0.8$], we have demonstrated that our framework is qualitatively consistent with the literature in terms of how MW-like ASHs form in the context of Λ CDM (Bullock & Johnston 2005; Cooper et al. 2010; Deason et al. 2016; Monachesi et al. 2019; Proctor et al. 2024).

B. INPUT FEATURE / TARGET VARIABLE CORRELATIONS

For completeness, Figure 16 shows contour plots of the three target variables (z_{50} , N_{90} and $M_{\text{acc}}^{\text{MMP}}$) vs. the three observable input features (M_{cen} , M_{ASH} and M_{sat}) defined in the main text and used in the Random Forest Regression described in Section 4. In each panel, contours indicate the 16-84, 5-95 and 1-99 percentiles of the distributions, with different colors corresponding to the three different merger tree samples, as indicated. The corresponding Spearman rank-order correlation coefficients are listed in Table 2. See the main text for a discussion of the various correlations.

This paper was built using the Open Journal of Astrophysics L^AT_EX template. The OJA is a journal which provides fast and easy peer review for new papers in the astro-ph section of the arXiv, making the reviewing process simpler for authors and referees alike. Learn more at <http://astro.theoj.org>.

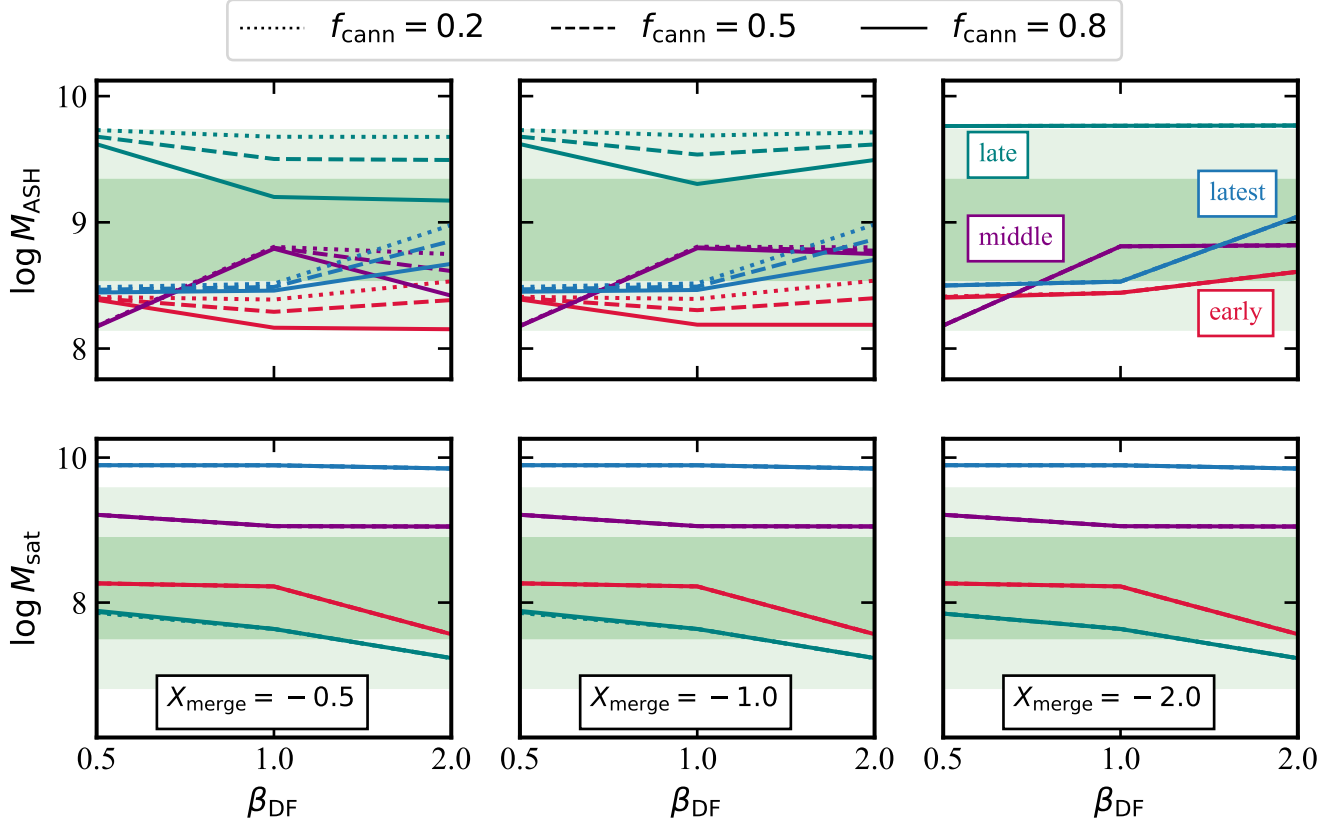


Figure 15. The impact of our three free parameters: dynamical friction strength (β_{DF}), merging criterion (X_{merge}), and cannibalization fraction (f_{cann}) on the four illustrative merger trees introduced in Section 3.5. For each tree, we explore $\beta_{\text{DF}} = [0.5, 1, 2]$, $X_{\text{merge}} = [-0.5, -1, -2]$, and $f_{\text{cann}} = [0.2, 0.5, 0.8]$, yielding 27 unique parameter combinations. The *early* tree is shown in crimson, the *middle* in purple, the *late* in teal, and the *latest* in blue. **Top Row of Panels:** The M_{ASH} component as a function of β_{DF} . **Bottom Row of Panels:** The M_{sat} component as a function of β_{DF} . The different columns correspond to different values of X_{merge} , while line styles indicate f_{cann} . Shaded regions show the 16-84 and 5-95 percentile extents of the corresponding S_0 mass distributions. Despite substantial tree-to-tree variation in the absolute mass components, the relative response of M_{ASH} and M_{sat} to changes in β_{DF} , X_{merge} , and f_{cann} is modest, indicating that stochasticity in merger histories dominates over systematic effects from parameter choices.

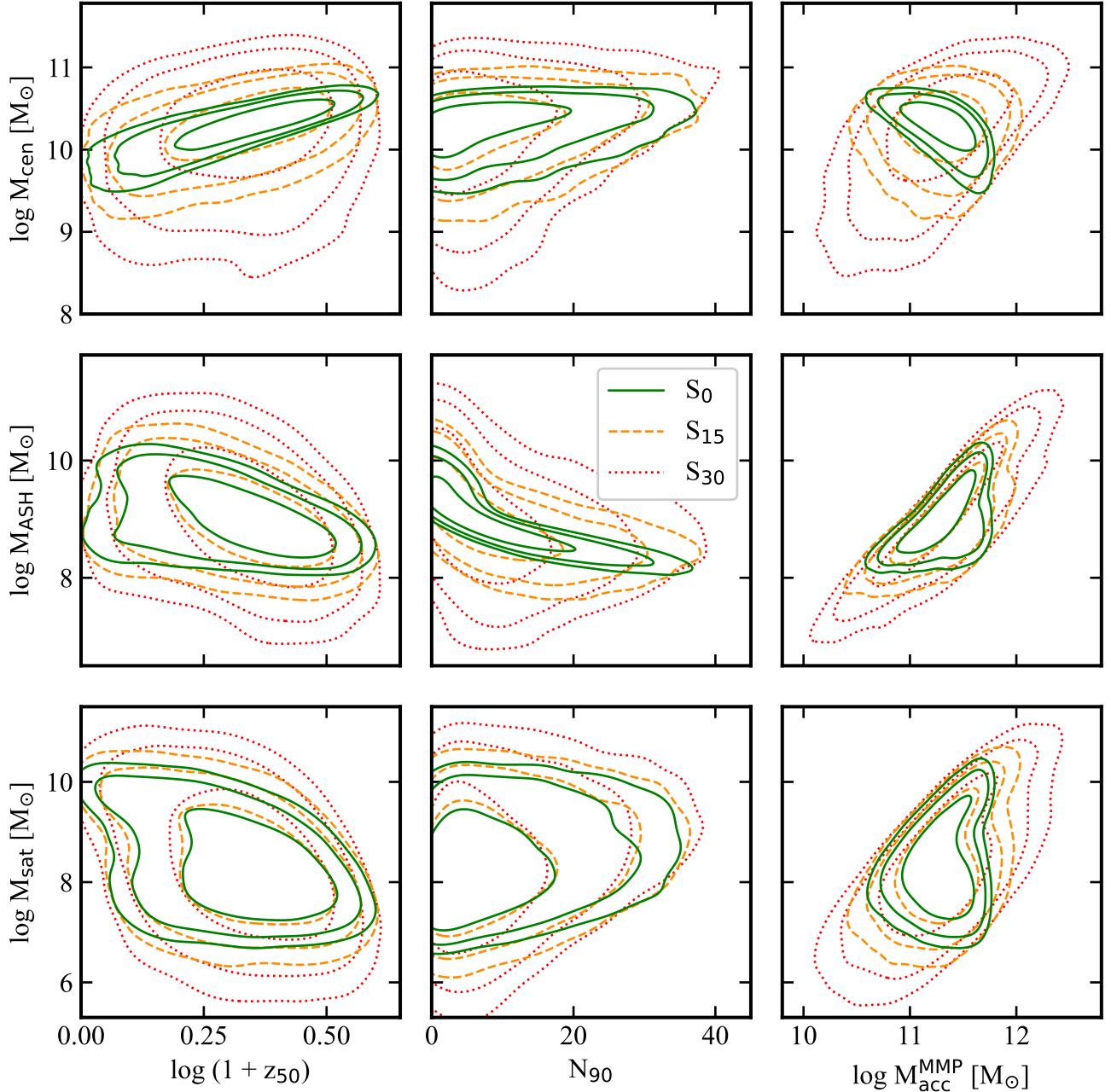


Figure 16. 2D contour plots showing the correlations between input features and target variables. The different lines indicate the 16-84, 5-95 and 1-99 percentiles of the distributions. As always, the three different merger tree samples distinguished by color according to the legend. For clarity, all associated rank-order correlation coefficients (ρ_S) are listed in Table 2. In this 3x3 grid, each column represents the mapping that the RFRA is attempting to learn. Notice that, in general, including host halo mass-mixing in the modeling weakens correlations.